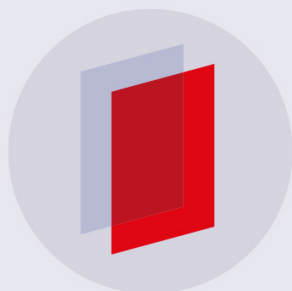


PAPER • OPEN ACCESS

Modeling cell intercalation during *Drosophila* germband extension

To cite this article: Lim C Siang *et al* 2018 *Phys. Biol.* **15** 066008

View the [article online](#) for updates and enhancements.



IOP | ebooks™

Bringing you innovative digital publishing with leading voices to create your essential collection of books in STEM research.

Start exploring the collection - download the first chapter of every title for free.

Physical Biology

OPEN ACCESS**PAPER**

Modeling cell intercalation during *Drosophila* germband extension

RECEIVED
23 April 2018**REVISED**
30 June 2018**ACCEPTED FOR PUBLICATION**
6 August 2018**PUBLISHED**
6 September 2018Lim C Siang¹ , Rodrigo Fernandez-Gonzalez^{2,3,4} and James J Feng^{1,5,6} ¹ Department of Chemical and Biological Engineering, University of British Columbia, Vancouver, BC, V6T 1Z3, Canada² Institute of Biomaterials and Biomedical Engineering, University of Toronto, Toronto, ON, M5S 3G9, Canada³ Department of Cell and Systems Biology, University of Toronto, Toronto, ON, M5S 3G5, Canada⁴ Developmental and Stem Cell Biology Program, The Hospital for Sick Children, Toronto, ON, M5G 1X8, Canada⁵ Department of Mathematics, University of British Columbia, Vancouver, BC, V6T 1Z2, Canada⁶ Author to whom any correspondence should be addressed.E-mail: james.feng@ubc.ca

Original content from this work may be used under the terms of the [Creative Commons Attribution 3.0 licence](https://creativecommons.org/licenses/by/3.0/).

Any further distribution of this work must maintain attribution to the author(s) and the title of the work, journal citation and DOI.

**Keywords:** planar cell polarity, T1 transition, rosettes, mathematical modelingSupplementary material for this article is available [online](#)

Abstract

Germband extension during *Drosophila* development is primarily driven by cell intercalation, which involves three key components: planar cell polarity, anisotropic myosin contractile forces on cellular junctions, and cellular deformation and movement. Prior experimental work probed each of these factors in depth, but the connection between them remains unclear. This paper presents an integrated chemomechanical model that combines the three factors into a coherent mathematical framework for studying cell intercalation in the germband tissue. The model produces the planar cell polarization of key proteins, including Rho-kinase, Bazooka and myosin, the development of anisotropic contractile forces, and subsequent cell deformation and rearrangement. Cell intercalation occurs through T1 transitions among four neighboring cells and rosettes involving six cells. Such six-cell rosettes entail stronger myosin-based contractile forces, and on average produce a moderately larger amount of germband extension than the T1 transitions. The resolution of T1 and rosettes is driven by contractile forces on junctions anterior and posterior to the assembly as well as the pulling force of the medial myosin in the anterior and posterior cells. The global stretching due to posterior midgut invagination also plays a minor role. These model predictions are in reasonable agreement with experimental observations.

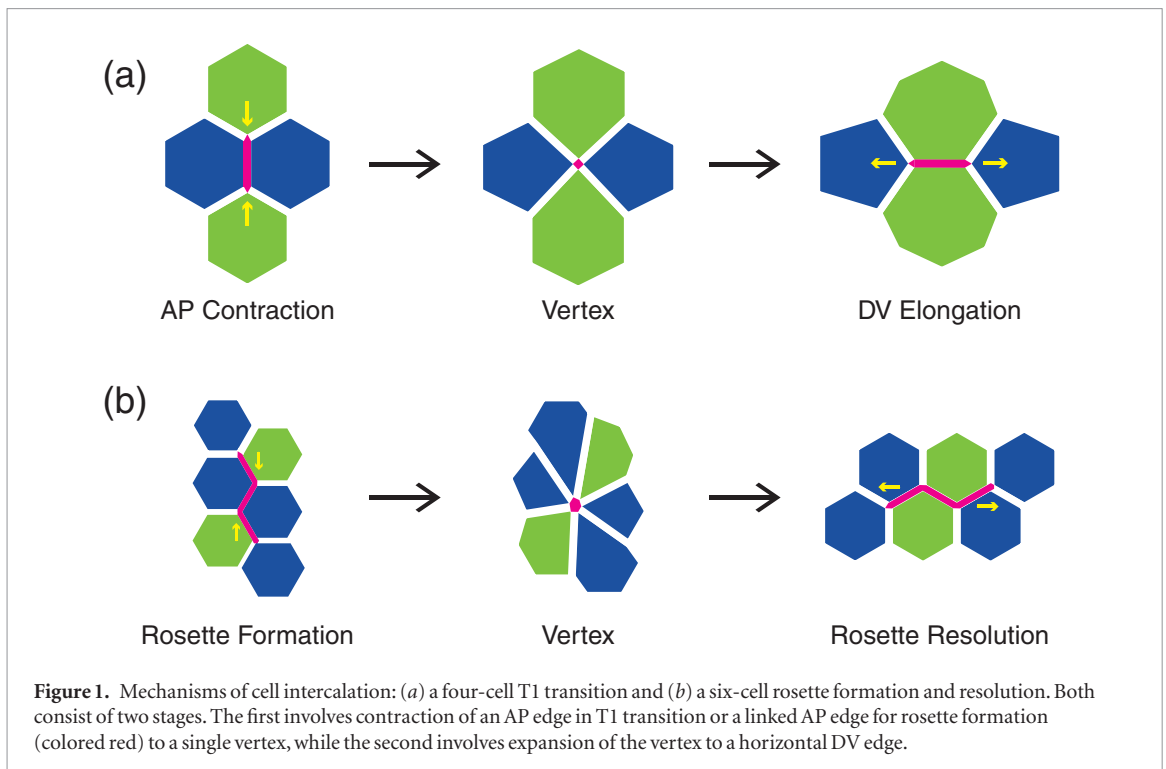
1. Introduction

During development of the *Drosophila* embryo, a morphogenetic process known as axis elongation establishes the fly's anterior–posterior (AP) axis. The germband, a monolayer of cells that eventually develop into the segmented trunk, converges along the dorsal–ventral (DV) axis while extending along the AP axis, approximately doubling its length in the end. Cell intercalation is the primary cause of this convergent extension [1]. Localized cellular behaviors such as cell-shape changes [2, 3] and oriented cell division [4], and tissue-scale forces due to posterior midgut invagination [5, 6] and unipolar enrichment of myosin at parasegmental boundaries [7] also contribute to the germband extension process.

Cell intercalation is realized through the T1 transition and rosette formation and resolution [8, 9]. In a T1 transition, four cells exchange neighbors to elongate the

cluster's dimension in the AP direction while shrinking it in the DV direction (figure 1(a)). Rosettes involve a greater number of cells that contract along a common axis into a flower pattern, and then resolve by elongating in the transverse direction (figure 1(b)). Both transformations consist of active contraction of cell borders perpendicular to the AP axis, conventionally called the AP edges, and extension of cell borders perpendicular to the DV axis, known as the DV edges. However, because rosettes involve contraction of more than one cell interface into a common vertex, they require coordinated contractile behaviors [10]. The relative importance of the two processes to cell intercalation is an open question [6, 11]. But rosette appears to be the more intensive of the two, as it requires stronger contractile forces along the AP edges [10], and results in greater change in aspect ratio for the assembly of cells [9, 11].

Cell intercalation has a biochemical aspect and a mechanical aspect. The former consists in the pla-



nar cell polarization (PCP) of several proteins, with the accumulation of Abl, Shroom, F-actin, nonmuscle myosin-II (Myo-II) and Rho-kinases (Rok) on the AP edges and apparently antagonist proteins such as Bazooka (Baz), E-cadherin (E-cad) and β -catenin on the DV edges [12–14]. The mechanical aspect is manifested by the contraction and elongation of cell borders, the rearrangement of cells and the overall deformation of the germband. These two aspects are closely coupled together. PCP is a pre-condition for the mechanics of intercalation; it generates the actomyosin apparatus for anisotropic contraction of cell edges [9, 15]. Meanwhile, the mechanics feeds back to the biochemistry through tension-regulated myosin dynamics [10, 16]. Interestingly, apart from enabling myosin contraction, PCP also contributes directly to cell intercalation by actively remodeling the adherens junctions (AJs) between cells. On a contracting AP edge, Rok downregulates adhesion [17], and antagonizes Baz that maintains and stabilizes AJs [18]. Besides, Abl enrichment promotes turnover of the AJ protein β -catenin [13]. All three pathways lead to AJ disassembly on contracting AP edges. On DV edges, on the other hand, Baz facilitates the apical localization of E-cad and β -catenin, and stabilizes the adherens junctions [9, 11, 19]. Thus, PCP can promote contraction of AP edges and the growth of the nascent DV edges.

Over the past decade, the mechanical and biochemical aspects have been studied in depth separately, leading to many useful insights, e.g. on the origin of planar cell polarity [7, 20] and the nature of the contractile forces [21–23]. But the two are rarely examined together despite ample evidence for their influencing each other. Lan *et al* [24] made a tentative step in this

direction, by integrating the biochemistry of planar cell polarization and the mechanics of cell deformation in a highly idealized four-cell setup. This model captures several features of experimental observations of T1 transition, including certain quantitative data such as AP/DV polarity and the magnitude of convergent extension. Its prediction of the mechanism for DV elongation has been confirmed by later experiments [6, 22]. While a useful first step [23, 25, 26], Lan *et al*'s model suffers from several fundamental limitations. Four cells are the minimum to realize the T1 transition, but cannot represent rosettes at all. The setup also fails to reflect the spatial expanse of the germband and the apparent stochasticity in when and where T1 transitions happen during germband extension. Moreover, it neglects interaction with the surrounding tissue, as well as the tissue-scale stretching due to posterior mid-gut invagination (PMI).

As an outgrowth from the model of Lan *et al* [24], the present work seeks to address its limitations. By adopting a 52-cell setup for the germband (figure 2), we introduce spatial and temporal stochasticity by randomly selecting AP edges on which to induce the onset of PCP. To represent the effect of the surrounding cells, we connect the model tissue to an outer boundary with cables bearing constant tension, and also impose a constant pre-tension on all cell edges according to experimental evidence [21]. PMI will be implemented according to experimentally measured extension rates [5]. Besides, the new model allows rosette formation and resolution; they arise when, by chance, two nearby AP edges are both selected to undergo contraction. Finally, we will also include the effect of AJ remodeling on AP and DV edges.

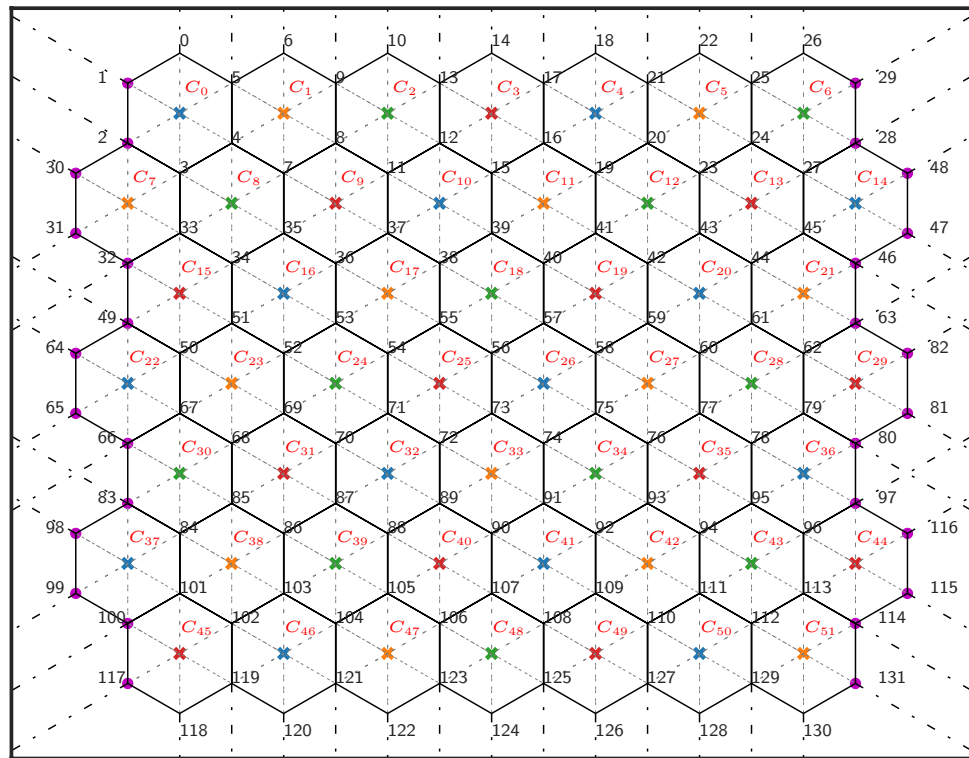


Figure 2. Geometry of the 52-cell tissue, with all the cells and vertices labeled. The cell centroids are represented by coloured crosses, with the phase lag $\phi = 0, \pi/4, \pi/2$ and $3\pi/4$ for blue, orange, green and red, respectively. The external cables, shown as dashed lines attached to the vertices of the tissue boundary, are initially aligned with the various spokes or edges. The magenta-colored boundary vertices are subjected to an additional outward movement due to PMI.

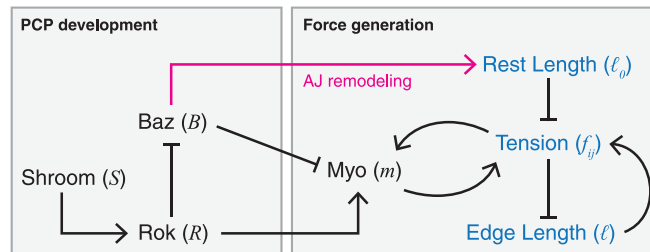


Figure 3. Schematic showing how the model generates PCP and contractile forces on cell edges. On a contracting AP edge, the elevated Shroom enriches Rok, which in turn depresses Baz and activates myosin. On DV edges, Baz suppresses myosin and promotes AJ buildup via the rest length (details of AJ remodeling in section S1 of the online supplemental information (stacks.iop.org/PhysBio/15/066008/mmedia)). Myosin and tension are linked in a positive feedback.

2. Model description

The initial configuration of our 52-cell germband tissue is depicted in figure 2. Each cell is initially a perfect hexagon with 6 vertices and 6 edges. On each cell edge we define 4 proteins: Shroom, Rok, Myo-II and Baz; the edge can lengthen or shorten according to the myosin contractile force and a linear elasticity. Within each cell, six spokes connect the vertices to the centroid of the cell. Based on experimental observations [3, 15, 27], we impose pulsating medial myosin on the centroid that pulls on the vertices along the spokes. The position of the centroid is updated at each time step as the cell deforms. With the current setup, it is relatively easy to generalize to larger tissues, at the expense of longer computing time.

2.1. Kinetic model

Our kinetic model is based on experimental observations of the biochemical pathways leading to PCP [9, 13, 14, 18], the mechanisms of AJ remodeling [9, 11, 13, 19] and a tension-myosin positive feedback [10, 16, 24]. Figure 3 depicts these interactions schematically. By tracking the amount of Shroom (S), Rok (R), Myo-II (m) and Baz (B) on each cell edge, the model predicts polarization of those proteins and in turn an anisotropic contractile force on AP edges. On each edge, the evolution of these species are governed by the following differential equations:

$$\frac{dR}{dt} = q_r - k_r e^{-S} R, \quad (1)$$

$$\frac{dB}{dt} = q_b - k_b RB, \quad (2)$$

$$\frac{dm}{dt} = k_1 R - k_2 m B - k^- m, \quad (3)$$

where for S we impose an anisotropic, time-independent level on the AP, DV and slanted ('shoulder') edges [14, 24]. The terms and the parameters are as explained in [24], with each unit of S , m , R and B consisting of 162 molecules of the respective protein. In particular, the e^{-S} form in equation (1) is chosen for mathematical convenience, the real kinetics of the Shroom-Rok chemical pathway being unclear at present. Note that $k^- = k_3 e^{-k_4 f}$ is a myosin detachment rate that is suppressed by tensile force f on the edge, a well-known positive feedback between junctional myosin and tension [10].

We model the pulsating medial actomyosin network by imposing a sinusoidal myosin signal on the centroid of each cell:

$$m_m = A_m \sin^2 \left(\frac{t\pi}{T} + \phi \right). \quad (4)$$

Although the cyclic contraction of medial actomyosin is an interesting phenomenon in its own right [15], it is not a central element in the current model, and is therefore modeled ad hoc. The phase angle ϕ is specified for each cell in the tissue (see figure 2) such that the neighbors exhibit anti-correlation on average, in agreement with experimental observations [15]. See the online supplemental information (SI), section S2 for more details on the neighbor-neighbor correlation for medial myosin.

2.2. Mechanical model

As in previous vertex models, the cells deform and move through the over-damped motion of its vertices:

$$\eta \frac{d\mathbf{x}_i}{dt} = \sum_j f_{ij} \frac{\mathbf{x}_j - \mathbf{x}_i}{|\mathbf{x}_j - \mathbf{x}_i|} + \sum_k \mathbf{f}_{ik} + \sum_k \mathbf{p}_{ik}, \quad (5)$$

where η is an effective viscosity, \mathbf{x}_i is the position of the i th vertex, f_{ij} is the total force on the edge connecting vertices i and j , \mathbf{f}_{ik} is the medial myosin force from neighboring cell k pointing toward its centroid, and \mathbf{p}_{ik} is a pressure force in cell k along the outward 'normal direction', which bisects the polygonal corner at i . Each cell edge exhibits a passive elastic force and a myosin-based active contractile force:

$$\mathbf{f}_{ij} = \mu(l_{ij} - l_0) + \beta m_{ij}, \quad (6)$$

where μ is the elastic modulus of the edge, l_{ij} and l_0 being its current and resting length, m_{ij} is the Myo-II level on the edge, and β is the myosin force constant [24]. The magnitude of the medial myosin force is simply $|\mathbf{f}_{ik}| = \beta m_{mk}$, m_{mk} being the medial myosin of cell k , and that of the pressure force is $|\mathbf{p}_{ik}| = \alpha(A_0 - A_k)$, A_0 and A_k being the resting and current cell area of neighbor k , and α the bulk modulus for the cell.

Besides mechanical forcing, remodelling of AJs is another factor in the contraction of AP edges and elongation of DV edges. The exact mechanisms for the remodeling are not clear at present, but several plausible pathways have been suggested, involving Rok, Abl, Baz, β -catenin and E-cad [11, 13, 18]. Among these, only Rok and Baz are accounted for in our model, and they localize to complementary cell borders upon onset of PCP [24]. We have chosen Baz to be the variable through which to encode AJ remodeling, as Baz exhibits similar polarization patterns to β -catenin and serves as a good surrogate for the latter [13]. In turn, the strength of AJs is modeled by passive elasticity on each edge, with a resting length $l_0(B)$ that varies with Baz. On AP edges, therefore, l_0 shortens with declining Baz and thus facilitates contraction of the edge, while on DV edges, l_0 grows with Baz to facilitate DV elongation. More details can be found in section S1 of the online SI.

Finally, the geometric, kinetic and mechanical parameters are evaluated from experimental data where possible. These are tabulated in SI (section S3) with sources and justifications. The numerical techniques for the computation are also discussed in SI.

2.3. Treatment of tissue boundaries

The 52-cell assembly of figure 2 represents only a portion of the real germband. Unlike in whole-embryo models [28], we need to treat the outer boundaries of the model tissue so as to mimic the interaction with the surrounding tissue in reality. As the germband does not exhibit spatial periodicity, it would be erroneous to impose periodic boundary conditions. Modeling the surrounding tissue by elastic springs attached to a fixed circular boundary produced poor results in Lan *et al* [24]. The springs hindered the contraction along the DV axis and extension in the AP axis and skewed the convergent extension of the tissue. In reality, the surrounding tissue would be undergoing convergent extension as well, and its deformation would accommodate that of the model tissue. To represent this interaction, we have introduced 'cables' emanating from the boundary nodes more or less isotropically (figure 2), each carrying a constant tension (to be defined in the next subsection). As the boundary vertices move, the cables shift as well, without changing their orientation.

In addition, PMI exerts a stretching force on the germband along the AP axis. Lye *et al* [5] quantified this stretching not as external forces on the germband, but as shape change of the cells. Collinet *et al* [6] represented it as movement of the boundary along the AP axis. Following [5], we view the germband extension as comprising the effects of cell intercalation and cell-shape change due to PMI. Using their measurements, we convert the rate of cell-shape elongation into a rate of AP extension for the tissue, and add that, at each time step, onto the movement of the boundary vertices that results from the intercalary forces and external

cables. Thus, the global stretching due to PMI amounts to an additional horizontal outward movement on our boundary vertices. Details can be found in SI (section S4).

2.4. Protocol of simulation

It is convenient to first imagine an equilibrium state in which the tissue is in chemical and mechanical balance. Imposing a uniform Shroom level of $S_e = 0.5$ on all edges, we find a chemical equilibrium with $R_e = 0.659$, $B_e = 0.607$ and $m_e = 0.912$ on all edges. Force balance is achieved by having perfectly uniform hexagonal cells of edge length $l_e = l_0^{eq} + \tau_{pre}/\mu - \beta m_e/\mu$, with each edge carrying a uniform pre-tension τ_{pre} , $l_0^{eq} = l_0(B_e)$ being the resting length at equilibrium level of Baz B_e . On the boundary vertices, the pre-tension is balanced by the external cables. See SI (sections S1, S3 and S4) for detailed discussion on choosing the values of l_0 , τ_{pre} and the cable forces F_{cable} to ensure mechanical equilibrium prior to the onset of cell intercalation.

The procedure for simulation is as follows. For the initial period, up to $t = 400$ s, we maintain the uniform $S_e = 0.5$, $R_e = 0.659$ and $B_e = 0.607$ on all edges. The medial myosin pulse is applied with phase lags among neighboring cells as prescribed in figure 2. Thus, the cells oscillate gently during this period, with no cumulative changes or polarization. Because of the positive feedback of junctional tension on myosin, the junctional myosin will oscillate about a mean value slightly below m_e thanks to the additional compression on the cell edge by the medial myosin.

At $t = 400$ s, we initiate the PCP by randomly selecting an AP edge by the stochastic scheme described in the next subsection, and raising S to 1 on it to initiate polarization and AP contraction. In the mean time, we assign an intermediate $S = 0.625$ on shoulders connected to the contracting AP edge. As new DV edges are created, from T1 transition or rosette resolution, $S = 0.5$ is assigned on them. This anisotropic Shroom pattern is based on experimental observations [14], and is assumed to be time-independent throughout the simulation.

2.5. Temporal and spatial stochasticity

During germband extension, the contraction of AP edges appears at apparently random times and locations. Here we model temporal stochasticity as a Poisson process. The frequency parameter is estimated from experimental data [13] to be roughly 0.05 event of AP contraction per cell per minute (see details in SI, section S5). Note that the Poisson distribution thus designed yields the expected frequency of AP contraction only at the start of our simulation. The geometric regularity of our model tissue, with relatively few AP edges, means that the actual rate of AP contraction drops in time and fewer T1's and rosettes will have taken place in the end than indicated by the target frequency.

Spatial stochasticity is implemented by selecting a random *available* AP edge for each contraction. The term *available* refers to AP edges that are connected to at least 3 cells and have yet to begin contraction. An interior AP edge, with neither end vertex exposed to the outside, are connected to 4 cells, while those at the boundaries are connected to 3 or fewer cells. T1 swap is impossible with AP edges that are connected to 2 cells or 1 cell. We also impose a constraint that no boundary AP edge be selected if an interior AP edge is available. The reason is that a sequence of early contractions on the boundaries tend to make some cells concave and cause that part of the tissue to collapse. AP contraction typically culminates in neighbor swaps through T1 transition or rosette formation, to be discussed next.

2.6. T1 transition and rosettes

We have adapted the scheme for T1 transition of Lan *et al* [24]. When an AP edge contracts to a critical length of $l_c = 0.02l_e$, i.e. 2% of its equilibrium length, a neighbor swap is implemented by rotating the AP edge counter-clockwise into a new horizontal DV edge and reconnecting its vertices to the closest neighbors. Shroom is set to $S = 0.5$ on the nascent DV edge, in keeping with the observed anisotropy [14]. Different from Lan *et al* [24], however, we do not set $m = 0$, $R = 0$ and $B = 0$ on the nascent DV edge. Instead, the DV edge carries over all the protein levels from before the rotation. This is because the model of Lan *et al* [24] lacked any treatment of the establishment of cell-cell junctions along the growing DV edge. As our model captures this effect via $l_0(B)$, we no longer need to make these drastic assumptions.

Rosettes form after two adjacent AP edges and the shoulder edge in between contract to a single vertex (figure S3). We model the initiation of rosettes as a stochastic process. If, by chance, two AP edges connected to the same shoulder edge are selected successively to contract, we use a second Poisson distribution to determine whether a rosette should form. If an affirmative answer is returned, Shroom is elevated to $S_m = 1.4$ on the two AP edges as well as on the shoulder sandwiched in between such that the 3 edges form a 'linked AP edge' [9, 10]. Its contraction to a single vertex then produces a six-cell rosette. To our knowledge, the only previous vertex model that accounted for rosettes is Trichas *et al* [29], for the mouse visceral endoderm. In experiments, rosettes made of 5–11 cells have been reported [9]. For simplicity, however, we restrict our model to six-cell rosettes only. The frequency parameter in the second Poisson process is estimated from *in vivo* data of Tamada *et al* [13], at 0.026 rosette per cell per minute (see details in SI, section S5), about half the rate of formation for T1 transitions. An additional constraint is that a cell is barred from participating in two or more rosettes at the same time. This avoids the appearance of overlapping or neighboring rosettes, which the model fails to resolve properly owing to its

geometric simplicity. Note that *in vivo* the germband cells undergo multiple rounds of rosette formation, and neighboring and overlapping rosettes do occur [9].

Rosette resolution follows a similar scheme to the T1 transition described above. Once the linked AP edge has shrunk to a critical length of $l_c = 0.06l_e$, we replace it by a new horizontal DV edge, with neighboring vertices separated by a uniform distance of $0.02l_e$. The critical length is three times that for T1 transition since 3 edges are involved in the rosette formation. After the transformation, the cell edges are reconnected onto the new DV edge as explained in SI, section S6, so as to ensure a unique topological outcome. On these new DV edges we set the Shroom level to $S_e = 0.5$ according to PCP [14], and let Rok, Baz and Myo-II evolve according to the kinetic model.

3. Results and analysis

Certain features of the model prediction are similar to those in the previous model of Lan *et al* [24] for the four-cell assembly, such as the development of the PCP in terms of Rok, Baz and Myo-II distributions within each cell. These features will receive only a cursory mention in the following. We will focus on the novel features of the current model, including those that arise from the large expanse of the tissue and the formation and resolution of rosettes. To isolate the effects of T1 and rosettes, we first study a scenario of germband extension with T1 transitions only. Then we will focus on the formation and resolution of a single rosette. Finally, we study the tissue-wide properties during a full simulation that incorporates both T1 transition and rosettes.

3.1. Germband extension with T1 transition only

We start by simulating the intercalation in the 52-cell tissue that undergoes T1 transition only, without rosettes. Because of the medial myosin pulse (equation (4)), the cells exhibit a gentle oscillation for the initial 400 s of the simulation, before PCP and intercalation set in. This period corresponds to the early Stage 6 of experimental observations (e.g. figure 1 in Blankenship *et al* [9]), and is similar to what Lan *et al* [24] described using the four-cell assembly.

Starting at $t = 400$ s, we randomly select AP edges to start PCP, at the frequency mentioned above, until all available AP edges have undergone contraction and T1 transition. The whole process is shown in movie 1 of the SI. Most features of the T1 transition are similar to those predicted by Lan *et al* [24], and some details are given in section S7 of the SI. For example, the development of PCP produces a greater contractile force on the AP edge (figure S4). The AP contraction is driven mainly by the junctional myosin force against resistance of the shoulder forces, while DV elongation is driven by the medial myosin forces in the two cells anterior and posterior to the new DV edge as well as

the shoulder forces, mostly against the myosin force on the DV edge (figure S5). A new feature is the disassembly of the AJs on the contracting AP edges and the strengthening of AJs on the growing DV edge. Modulated through the resting length $l_0(B)$ of the cell edges, the declining elastic resistance on the AP edge promotes its contraction, while the lengthening l_0 on the DV edge relieves the elastic tension and facilitates DV elongation.

Over the course of the simulation, T1 transitions occur stochastically in space and time. To probe this stochasticity, we have run 10 independent simulations under identical conditions. Because of the regularity of the geometric setup, a total of 49 T1's take place in each run, and the tissue elongates to the same regular pattern (see movie 1). An interesting indicator of the stochasticity of the process is the times for AP contraction T_{AP} and DV elongation T_{DV} . For each AP contraction, we measure the time between the onset of PCP and the moment that the AP edge length shrinks to the threshold of $0.02l_e$. The duration of DV elongation is measured between the appearance of the new DV edge and the moment when the DV length first attains the equilibrium length of $l_e = 4 \mu\text{m}$. This treatment differs from that of Lan *et al* [24], whose DV edge length oscillated more or less regularly, and its third peak was taken to be the end of the elongation process. In the current model, the elongation of the DV edge is less regular and a third peak cannot be easily defined. Compiling T_{AP} and T_{DV} data for all the T1 transitions in the 10 simulations, figure 4 shows that both times exhibit a rather wide distribution. This is because AP contraction and DV elongation are affected by what the neighboring cells happen to be doing, and the latter varies stochastically thanks to the random selection of AP edges for contraction. After averaging all 490 T1's, we have mean values $T_{AP} = 493$ s and $T_{DV} = 304$ s. Experiments have recorded T_{AP} ranging from 450 to 600 s and T_{DV} ranging from 420 to 600 s [8, 9]. The predicted mean values are somewhat shorter than the measurements. Potential causes include the uncertainties in evaluating the parameters and in defining the start and end points of contraction and elongation. Besides, the broader distribution of figure 4 suggests that our model tissue is too small and sensitive to noise.

Next, we will examine the degree of anisotropy in terms of the distribution of the proteins and the contractile forces. Following prior experimental and modeling work [10, 14, 15, 18, 22, 24, 30], we focus on the ratio of these quantities between the AP and DV edges. In experiments, the level of various proteins are measured by averaging vertical or horizontal edges of differing lengths [21, 30]. These edges are presumably at different stages of T1 transition. To approximate the averaging in the experiments, we have taken the time average on AP edges from the onset of AP contraction to the T1 swap, and on DV edges from the T1 swap to the completion of DV elongation. Additionally, we have averaged among the T1 transitions for the

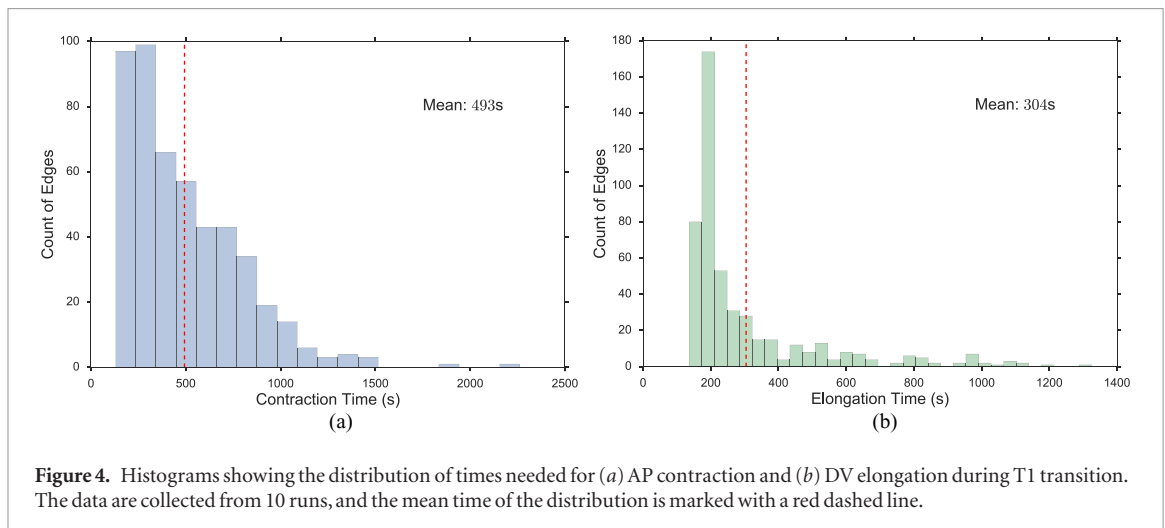


Figure 4. Histograms showing the distribution of times needed for (a) AP contraction and (b) DV elongation during T1 transition. The data are collected from 10 runs, and the mean time of the distribution is marked with a red dashed line.

Table 1. AP/DV ratios of various proteins and the edge force during T1 transition: comparison between model predictions and experimental measurements.

| | Experiments | Model of Lan <i>et al</i> [24] | This model |
|------------|--------------------------|--------------------------------|-----------------|
| Rok | 1.5–1.9 [14] | 1.65 | 1.38 ± 0.08 |
| Baz | 0.33–0.5 [14, 18, 31] | 0.607 | 0.81 ± 0.07 |
| Myo-II | 1.3–2.1 [14, 18, 27, 31] | 2.74 | 1.80 ± 0.40 |
| Edge force | 1.7–2.55 [10, 30] | 7.5 | 1.60 ± 0.70 |

10 realizations. The results are compared with prior experiments and modeling in table 1.

The AP/DV contrasts in Rok and Baz levels are somewhat weaker in our model than in the experiments, while the Myo-II contrast falls in the experimental range. Our force ratio is slightly below the experimental data, but is a marked improvement over the prediction of Lan *et al* [24]. Experimentally, the force ratio is estimated from the ratio of end retraction speeds after laser ablation of the cell edges. What is measured, therefore, is the total force on the edges, which in our model comprises the myosin and elastic contributions. Since Lan *et al* [24] did not consider the myosin tension on the nascent DV edges, they have over-predicted the ratio by a wide margin. In addition, a more precise comparison can be made of the magnitude of the edge forces. Bambardekar *et al* [30] have reported an average force of 0.324 nN on AP edges and 0.127 nN on DV edges. In comparison, our model predicts 0.68 nN and 0.46 nN, respectively, more than twice as high as the measured values. In the experiment, the force values were averaged over edges oriented within 45° of the AP or DV axis, and may have included various shoulder edges. In our model, the AP and DV edges are clearly defined. This may partially explain the discrepancy.

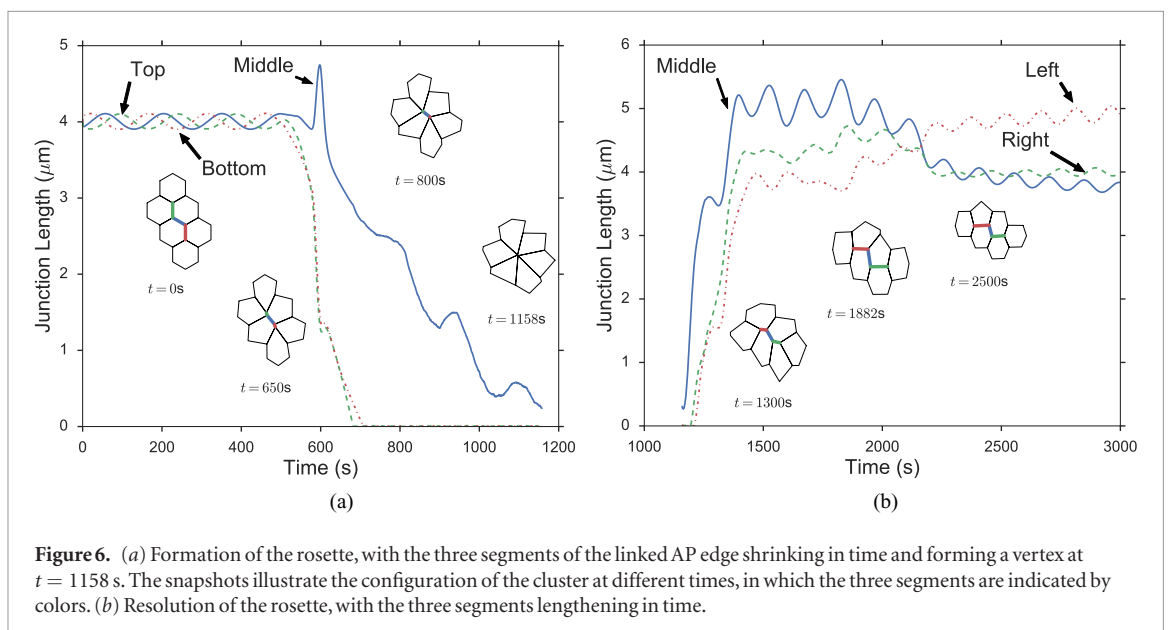
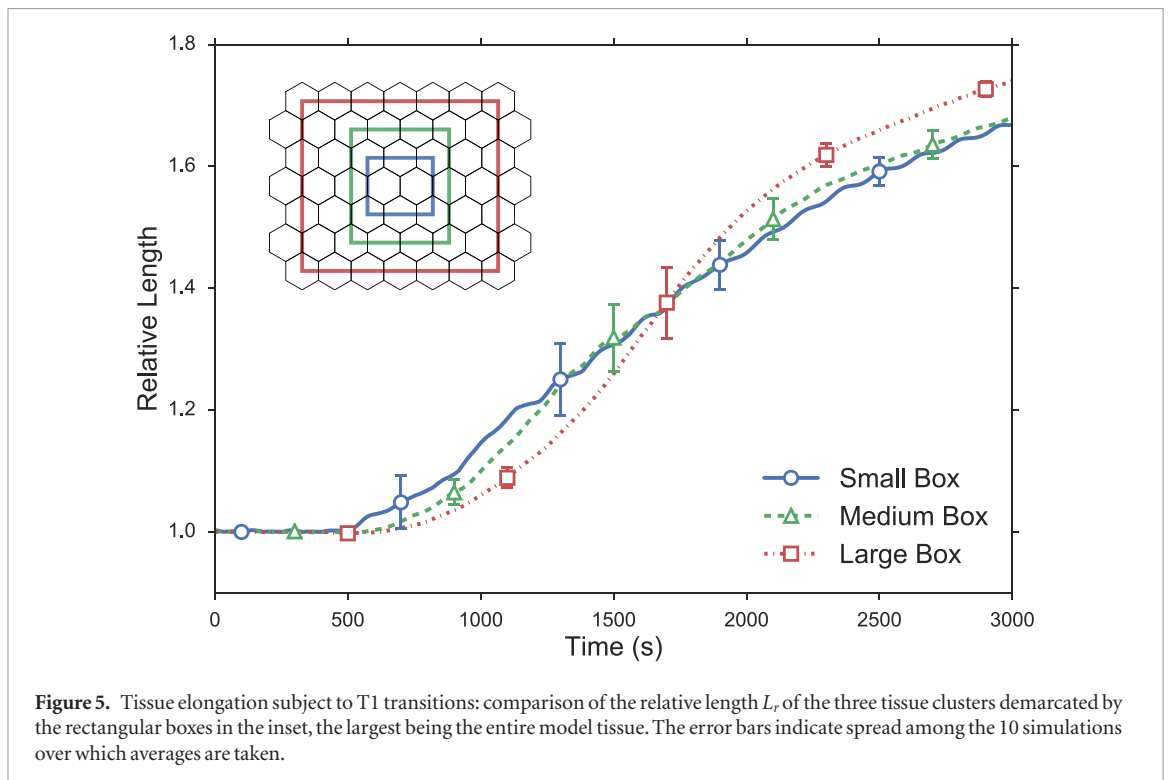
Finally, let us turn to the overall deformation of the tissue. Following Collinet *et al* [6], we define a relative length L_r as the current AP length of the tissue, measured between the centroids of the leftmost and rightmost cells, divided by the initial length before the

onset of axis elongation. Figure 5 shows the temporal evolution of L_r averaged over the 10 runs. The relative length of the model tissue (large box) rises to a value of $L_r = 1.74$ at the end of the simulation, roughly 40 min after the onset of intercalation. This compares with experimental measurements of $L_r = 2$ – 2.5 [1, 6]. *In vivo*, the germband undergoes many rounds of T1 and rosette processes. In our model tissue, the simple geometry allows fewer T1 transitions, and no rosettes in this case. These have contributed to the under-prediction of tissue elongation.

By comparing the relative deformation of cell clusters of different sizes, Collinet *et al* [6] observed that ‘tissue extension is spatially homogeneous and scale-independent’. That is to say, the strain is uniform throughout the tissue. To test for spatial homogeneity in our model tissue, we compare the relative length L_r of the three tissue clusters delineated in the inset of figure 5. The relative length agrees to within 4% at the end of the simulation among the three boxes. The earlier differences are mainly due to spatial variations of where a T1 happens first. Thus, our model has successfully recapitulated the spatial homogeneity that Collinet *et al* [6] demonstrated *in vivo*. Note further that the larger boxes show slightly larger elongation in figure 5, a feature that is also present in the experimental data (figure 1(e) of [6]). This may be related to the stretching along the AP axis due to midgut invagination, which, in our model at least, favors greater deformation of cells at the left and right edge of the tissue, as is evident from images near the end of movie 1. Interestingly, the effect of PMI on cell shape change is actually inhomogeneous *in vivo* [5]; cell deformation is more pronounced closer to the posterior tip of the embryo. As explained in section S4 of the SI, this feature is not included by our model.

3.2. Analysis of rosette formation and resolution

Now we allow both T1 and rosettes in the simulation. In this subsection, we examine closely the formation and resolution of the first rosette as a representative of all rosettes. The purpose is to discuss the various



mechanisms that can affect the rosette formation and resolution, and explore its local features. The global features of the full simulation, with both T1 and rosettes appearing and resolving with spatial and temporal stochasticity, will be discussed in the next subsection.

At the end of the initial oscillation, $t = 400$ s, we start to select randomly AP edges to initiate PCP and contraction, as described in the previous subsection. In the representative simulation that we will describe now, the first rosette appears when two nearby AP edges in the middle of the tissue, edges 19–41 and 42–59 in figure 2, are selected at $t = 499$ s and 501 s for contraction, respectively. Thus, S is raised to 1.4 on them and to 0.625 on the shoulders connected to them

on the outside. At $t = 538$ s, the sandwiched shoulder (41–42) is selected for rosette formation by a Poisson probability and S is raised to 1.4 on the shoulder as well. This causes contraction of the three connected edges, referred to as the linked AP edge following [9, 10] ($t = 650$ s in figure 6(a)). Note that when the two AP edges start to contract, the shoulder edge in-between is first elongated. With the development of its own Rok and myosin, however, it contracts as well until the linked AP edge shrinks down to the critical length of $l_c = 0.06l_c$ at $t = 1158$ s. After rotating the linked AP edge into the horizontal direction and reconnecting the vertices according to figure S3, the three nascent edges elongate (figure 6(b)). Interestingly, it is the middle edge that elongates most rapidly. The two hori-

zontal edges elongate more slowly, and DV elongation is complete when the shortest of the three reaches $l_c = 4 \mu\text{m}$ at $t = 1882 \text{ s}$. The forces driving and resisting the rosette transformation are the same ones as in T1 transition, but larger in magnitude (see section S7 and figure S6 of SI). Note that the topology of the cells after rosette resolution is identical to what would have resulted from two separate T1 transitions involving the two AP edges initially chosen to contract. The rosette formation and resolution are also shown in movie 2 in SI. During this process, the surrounding tissue undergoes stochastic T1 transition, and the second rosette has started at $t = 550 \text{ s}$ involving edges 34–51, 51–50, and 50–67.

To effect the remarkable contraction of the three linked edges into a vertex, our model has adopted the ad hoc device of raising the Shroom level on them. Experimental observations *in vivo* have identified several factors that may have contributed to this contraction. First, tension is known to suppress the detachment rate of myosin motors on actin filaments [10], and this amounts to a positive feedback between tension and myosin on a cell border. This factor has been incorporated into our model. Second, the protein Abl tends to intensify β -catenin turnover on AP edges, causing disassembly of cell junctions along the linked AP edge and facilitating its contraction [13]. This has been modeled via the resting length l_0 of the linked AP edges, which decreases as Baz becomes depleted. Without this effect, AP contraction would not be able to proceed to the point of producing a T1 transition or a rosette. The third is the alignment of several cell borders into a linked edge oriented perpendicular to the AP axis [9, 10]. This aligns the contractile forces on the connected segments so as to reinforce each other's effect. Experimental images and videos suggest that the fluid-like deformation of the germband and the irregular shapes of the cells frequently bring the edges to near alignment. In our model tissue, however, the regular hexagonal shape is such that it is difficult to align the shoulder edge within 30° of the DV axis. As a result, this factor is not well represented in our model. Fourth and finally, recent experiments suggest that stretching of a cell edge to a large strain or strain rate may predispose the edge to a strong surge of myosin recruitment afterwards [10, 32, 33]. We have tested this factor in our model by making the rates of myosin attachment and retention functions of the strain or strain rate (see SI, section S8 for more details). This at most provides an initial boost for myosin that disappears later with the AP contraction, as the strain and strain rates both decline. In reality, the reaction of a stretched cell edge may possess a certain memory or relaxation time. This remains to be explored using more sophisticated mathematical formulations.

Is the rosette more effective than T1 at elongating the tissue in the AP direction? Zallen and Blakeship [11] reported that ‘rosette formation amplifies the effects of neighbor exchange, producing a 5.5-fold

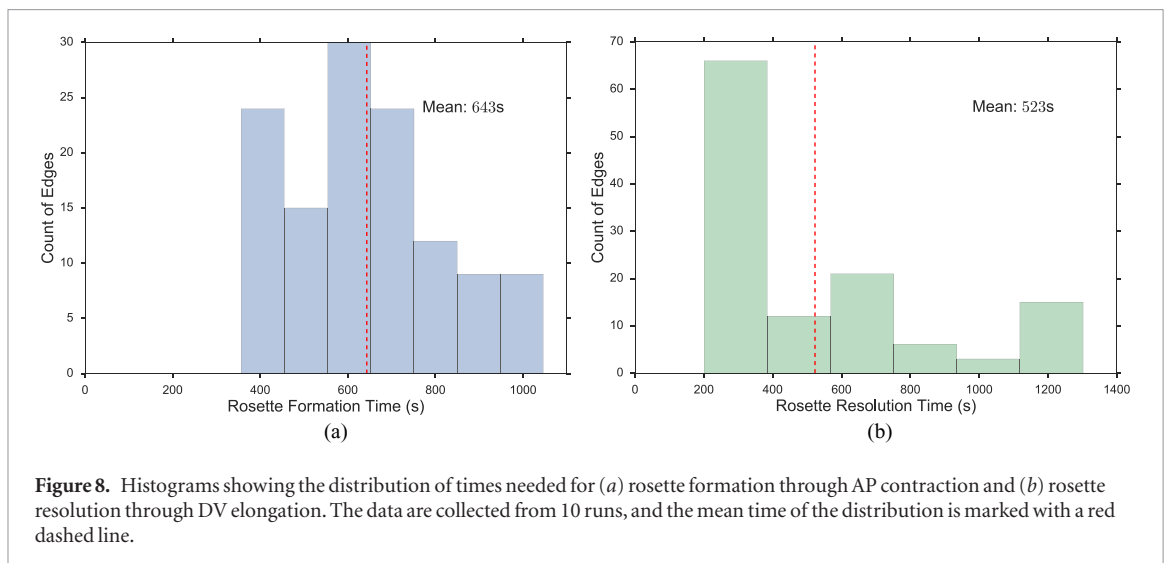
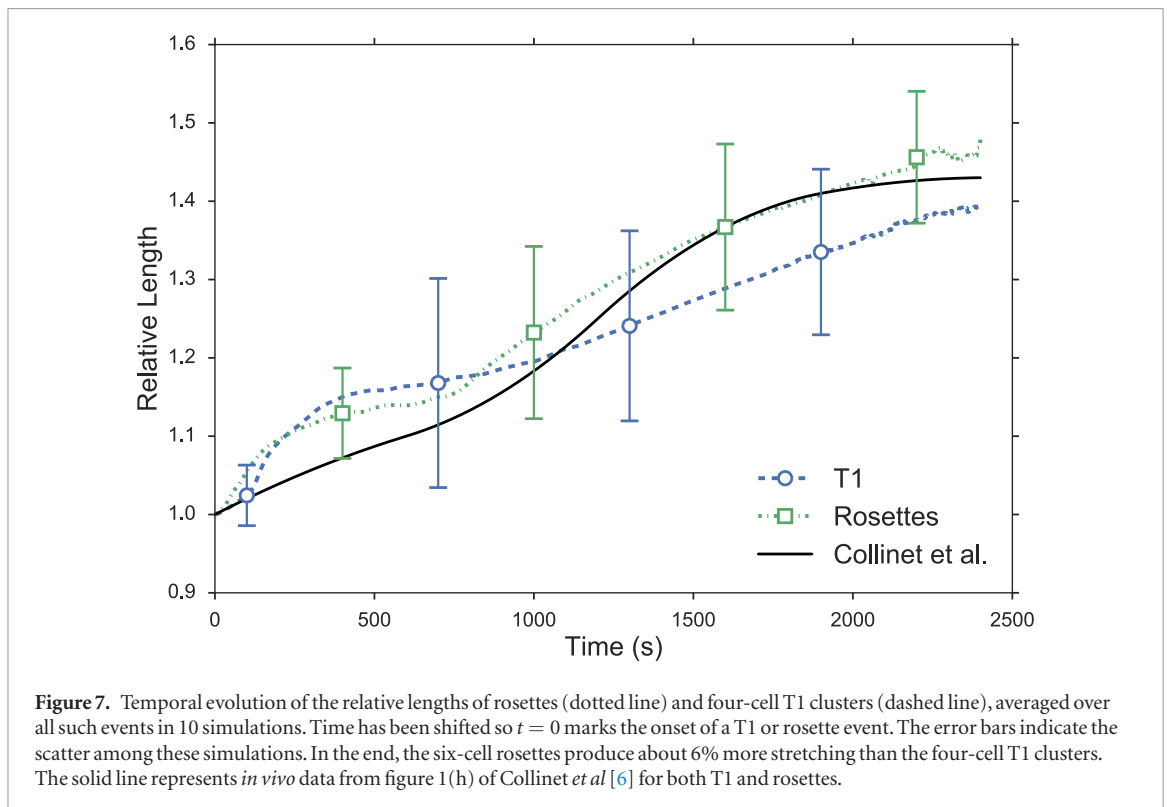
average change in the AP:DV aspect ratio, compared to a 2.5-fold average change for T1 processes’. When Collinet *et al* [6] measured AP extension associated with T1 and rosettes, they ‘did not find a significant difference (figures 1g, h)’. To probe this question using our model, we first note the different ways of measuring tissue elongation in the literature. Some researchers [9, 11, 24] use the change in the AP:DV aspect ratio, while others [6] use the relative length, as in figure 5 of this paper. As the extensional strain along the AP axis and the compressive strain along the DV axis have roughly the same magnitude [6, figure 1k], one can compare the relative length with the square root of the change in AP:DV aspect ratio. Besides, measuring the relative length from the outline of the cell cluster yields a smaller ratio than using the centroid of the outmost cells (see figure S1 of [6]), especially for smaller clusters. With these clarified, we can compare our model predictions with the experimental data.

Using the cell outlines, we have measured the evolving relative length L_r of four-cell clusters during T1 and six-cell clusters during rosette transformation. After shifting the start of such events to $t = 0$, we compute an average L_r for the T1's and for the rosettes, and compare them with the measurements of Collinet *et al* [6] in figure 7. On average, the T1 clusters achieve a relative length of $L_r^{\text{T1}} = 1.39$ at the end, whereas the rosettes attains a somewhat stronger stretching at $L_r^{\text{ro}} = 1.48$. The data of Collinet *et al* [6] show little difference between the two structures, both attaining a relative length of $L_r = 1.44$ (figure 1(h) therein). Thus, our model indicates a moderate advantage to the rosettes in terms of tissue elongation.

How to reconcile the above with the apparently conflicting trends in experimental observations? Blakeship *et al* [9] offered a clue when they noted ‘a change in the AP/DV aspect ratio ... by a factor of 2.1 for rosettes of 6–7 cells ($n = 74$) and by a factor of 3.0 for rosettes of 8–10 cells ($n = 9$)’. The factor of 2.1 translates to a relative length of $L_r = \sqrt{2.1} = 1.45$, close to that of our six-cell rosette and that of Collinet *et al* [6], whose figure 1(g) shows rosettes of 6 cells. Therefore, it appears that rosettes involving a larger number of cells may produce significantly more stretching than T1's, while six-cell rosettes are only moderately more effective. Incidentally, the larger numbers reported by Zallen and Blakeship [11] are based on cell centroid positions, as opposed to the cell outlines. If one uses their figure 3 to estimate the conversion factor between these two measures, then their centroid-based data—5.5-fold for rosettes and 2.5-fold for T1—translate to 2.94 and 1.57, respectively, for the outline-based measure of change in aspect ratio. These are consistent with the data of Blakeship *et al* [9].

3.3. Full simulation with both T1 transitions and rosettes

Having analyzed the T1 transition and rosette transformation separately, we turn now to tissue-



wide features of the simulation with both processes occurring. Again, we have carried out 10 realizations from identical initial conditions. Their outcome are qualitatively similar but quantitatively different thanks to the temporal and spatial stochasticity built into the model. We will average among the 10 runs to measure the various aspects of tissue elongation.

Movie 3 in the SI depicts a representative run of the full simulation, which lasts 3000 s with 41 T1 transitions and 4 rosettes during the simulation. On average, the AP contraction phase of a T1 transition takes 438 s, while the DV elongation phase 270 s. These are close to the times in the simulations of figure 4 with only T1 transitions. Rosette formation and resolution take considerably longer times (figure 8). The formation and resolution times of 643 s and 523 s compare

with experimental values of 648 s and 600 s [9]. As noted earlier, the broad distributions of the contraction and resolution times reflect the stochastic disturbance from the neighboring cells that may delay or precipitate cell intercalation.

Depending on how nearby AP edges are chosen randomly to form rosettes, the total numbers of rosettes and T1 transitions vary among our 10 simulations, the number of rosettes ranging from 4 to 6 while that of T1 from 37 to 41. These are much lower than those recorded *in vivo* [13, 31]; based on the more recent experimental data of [31] one would expect some 35 rosettes and 63 T1s for 52 cells. Furthermore, the final configuration is always the same in the simulation, with hexagonal cells in neat rows. Both features are symptomatic of the simple and regular configuration of our

Table 2. Anisotropy of various protein species and the edge force: comparison between model predictions and experimental measurements. The AP:DV ratio corresponds to edges in T1 transitions, while Linked AP:DV refers to edges in rosettes.

| | Experiments AP:DV | Experiments Linked AP:DV | This model AP:DV | This model Linked AP:DV |
|------------|-------------------------------|-----------------------------|---------------------|----------------------------|
| Rok | 1.5–1.9 [14] | (No data) | 1.35 ± 0.09 | 1.99 ± 0.15 |
| Baz | 0.33–0.50 [14, 18, 31] | (No data) | 0.83 ± 0.08 | 0.54 ± 0.05 |
| Myo-II | 1.05–2.1 [10, 14, 18, 27, 31] | 1.14 [10] | 1.60 ± 0.40 | 3.70 ± 1.0 |
| Edge force | 1.7–2.55 [10, 30] | 2.9–3.1 [10, 15] | 1.40 ± 0.80 | 3.60 ± 1.30 |

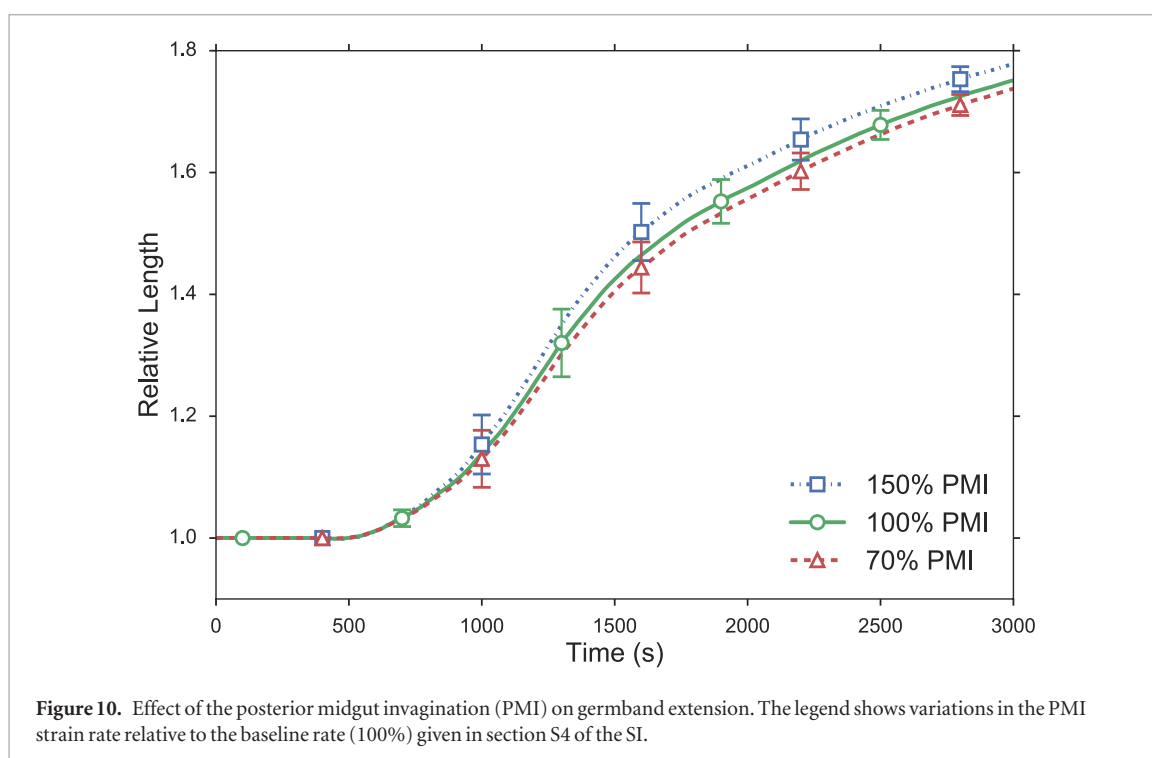
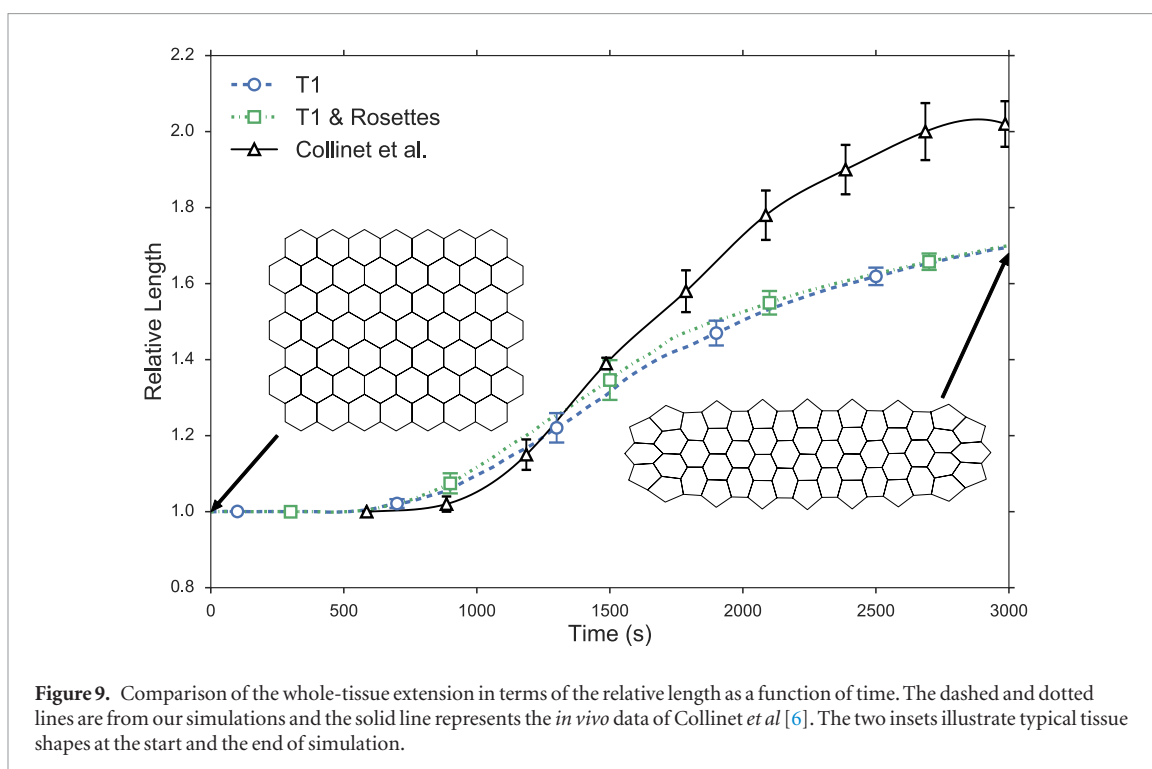
cells in the model tissue. The total numbers of T1 and rosettes are limited by the number of AP edges available. *In vivo*, cells exhibit considerable variations in shape, size and connectivity, and the germband flows and deforms in time to create new AP edges. Thus, the tissue undergoes multiple rounds of intercalation during germband extension [9]. This should be kept in mind when comparing our model predictions with experiments in the following.

Anisotropy in the distribution of Rok, Baz and Myo-II and the edge tension are tabulated in table 2, in comparison with experimental data in the literature. In the full simulation, the AP:DV ratios in T1 transitions are close to those in the T1-only simulations of table 1. What is of more interest here is the ratio between linked AP edges and DV edges in rosettes, computed by averaging the three linked edges. The Rok and Baz ratios are more strongly polarized than those in T1 transitions. They are also comparable with experimental data for AP:DV ratios, although the experimental sources [14, 18, 31] did not distinguish between T1 and rosettes, and probably contained both. In our model, the linked AP edges exhibit a Myo-II level more than twice that of isolated AP edges. Partly this is due to the elevated Shroom level on linked AP edges. Moreover, Myo-II enjoys a positive feedback with tension [10]. The strong tension on the linked AP edges has given Myo-II an additional boost. Again, most experimental reports did not distinguish the linked and isolated AP edges. For example, Farrell *et al* [31] reported an AP:DV myosin ratio of 2.1 for both types of AP edges. Besides, this ratio includes edges within 15° of the vertical and horizontal axes. Considering these two factors, the real linked AP:DV ratio for myo-II *in vivo* is likely much higher than 2.1. The only experimental study that distinguishes myosin levels on linked and isolated AP edges gives the following ratios [10]: linked AP:AP:DV = 1.14:1.05:1. Though the ratios are lower than in the other reports [14, 18, 27, 31], the linked AP edge still exhibits a clear advantage over the isolated AP edge in terms of myosin enrichment relative to the DV edge. Note that the strain-activated myosin recruitment mechanism may have contributed to the myosin enrichment on linked AP edges in the experiments [33]. Finally, the model successfully captures the strong tension force on linked AP edges, relative to isolated AP edges, and the tension ratio is not far above data gathered from laser ablation experiments [10, 15].

Figure 9 compares the model predictions of the tissue stretching for the T1 only simulations of section 3.1 and the full simulations of this section. The *in vivo* data of Collinet *et al* [6] are also shown for comparison. First, the inclusion of rosettes in our model leads to a slight increase in the germband extension, consistent with the observations in figure 7. The effect is weak because the simulation sees much fewer rosettes than T1's. Second, our model predictions of relative length fall some 15% below the *in vivo* data. In the end, our relative length L_r reaches about 1.7, whereas *in vivo* L_r rises above 2. The reason for this discrepancy, as alluded to already, lies in the fact that the simple geometry of our model tissue allows just one round of intercalation, after which no vertical AP edge remains and no further intercalation can occur. *In vivo*, on the other hand, the germband undergoes complex overall deformation that allows movement and rotation of cell edges and multiple rounds of T1 and rosette processes. This is clear from videos of germband extension in Blankenship *et al* [9]. Therefore, the simplicity of our model tissue has limited its ability to capture the true magnitude of germband extension.

To test the spatial homogeneity of stretching, we again compare the strain (or relative length) of the 3 rectangular clusters depicted in figure 5. Results show that such homogeneity remains in the full simulation; the relative length agrees to about 4% among the 3 boxes. This is perhaps no surprise given that the T1 transitions alone incur uniform deformation throughout the tissue (figure 5), and that rosettes produce only slightly larger tissue strain than T1, and are relatively few in our model predictions.

Finally, we discuss the effect of the 'extrinsic force' due to posterior midgut invagination (PMI) on germband extension [5, 6]. As explained in the SI (section S4), the PMI effect is imposed as a strain rate along the AP axis. If we use too low a strain rate in our model, the interior cells tend to develop concave shapes, possibly another symptom of the overly simple topological setup of the model tissue. This limits us to a relatively narrow range of variations for the PMI strain rate. Figure 10 shows that PMI contributes modestly to the total germband extension. With the PMI strain rate at 70% or 150% of the baseline value, the relative length at the end goes down by 0.8% or up by 1.5%, respectively. Thus, the model prediction is consistent with the consensus in the literature that germband extension is



mostly due to cell intercalation, but tissue-level external forces also contribute to it [5, 6, 10].

4. Conclusion

We present a mathematical model for cell intercalation during germband extension through two different mechanisms: T1 transition and rosette formation and resolution. Our model integrates the biochemistry of four protein species—Shroom, Rho-kinase, Bazooka and Myosin—with the mechanics of cell deformation and movement. It differs from prior vertex models

for tissue deformation and morphogenesis in that we do not prescribe mechanical rules governing cell-cell interaction. Rather we predict the mechanical outcomes, e.g. cell deformation and rearrangement, from the polarization of signaling proteins and anisotropic contraction forces.

Thus, our model strives to integrate insights extracted from previous experimental observations to predict the various features of germband extension. In particular, we recapitulate the three stages of cell intercalation: stochastic polarization of Shroom leading to the development of PCP; anisotropy in myosin forces

driving junctional contraction on the AP borders; and finally tissue-scale cell deformation and movement. Within the parameter ranges tested, the model predicts the following main results:

- (a) Planar cell polarity arises from a prescribed Shroom signal, with Rok and Myo-II localizing preferentially on AP edges and Baz on DV edges.
- (b) T1 transitions and six-cell rosettes take place stochastically, both in time and in space, throughout the simulation.
- (c) On average, a six-cell rosette transformation produces about 6% more tissue stretching than a four-cell T1 transition.
- (d) The germband tissue stretches in a spatially homogeneous fashion, with roughly uniform strain throughout the interior of the tissue.
- (e) Posterior midgut invagination makes cells at the anterior and posterior borders deform more than in the interior, but its overall contribution to tissue elongation is minor.

These model predictions are compared with experimental data. The degree of AP/DV polarity in forces and protein levels, the durations of AP contraction and DV elongation, and the amount of stretching for each T1 or rosette event are all in reasonable agreement with experimental observations.

However, the model under-predicts the total amount of tissue stretching by nearly 20%. This is because of the simplistic geometric setup of our model tissue. With a regular initial lattice of identical hexagonal cells, we pre-assign a limited number of AP edges, and cannot account for multiple rounds of T1 and rosette transformations as occur *in vivo*. Thus, the total number of T1 and rosette events are both much lower, on a per cell basis, than *in vivo*, and the total tissue stretching is too low.

We have noticed other symptoms of the geometric setup of the model tissue. With only 52 cells constrained by the forces posed on the edges, the cells are much more strongly coupled mechanically than in the real germband, which exhibits a good degree of fluidity in terms of the deformation and movement of the cells [34]. This artificial rigidity has several consequences. First, our cell edges do not rotate or align easily, and we cannot reproduce the aligned common edge as a precursor to rosettes, which is prevalent *in vivo* [9, 10], nor rosettes incorporating a larger number of cells. Instead, our six-cell rosettes are produced by an ad hoc scheme of elevating Shroom on nearby AP edges. Second, we cannot account for the progressive irregularization of the cell shapes as happens in reality [35]. Because of the regularity in the geometric setup, our cells typically return to perfect hexagons at the end. This tendency toward regularity also predisposes the cells to unrealistic shapes; they tend to become

concave in the tissue interior, especially if the pre-tension is low. Third, the model does not allow neighboring or overlapping rosettes, as they frequently fail to resolve properly. A solution to this series of flaws requires a tissue with a much larger number of cells that are less strongly coupled mechanically and less constrained by the forces at the boundaries. In addition, we may need to account for the strain-induced myosin recruitment mechanism reported recently [10, 33] and also incorporate more realistic mechanics and rheology of the epithelium.

Finally, it is important to note that our model focuses on the action of junctional myosin, and models the medial myosin in a simplistic way. Biological evidence shows that medial myosin flow may be a key player in germband extension [36–38]. Besides, the model also neglects potential effects of the cephalic furrow formation, which may have exerted additional elongation along the AP axis, complementing the PMI. Nevertheless, by extending the model of Lan *et al* [24], we present an integrated biochemo-mechanical model that links mechanical deformation to the kinetics of signaling proteins. Although far from completeness and perfection, this continues the effort of coupling biochemistry and mechanics to understand and predict morphogenetic processes involving the deformation and movement of cells.

Acknowledgment

JJF and LCS acknowledge support from the Natural Sciences and Engineering Research Council of Canada (2014-05862). The research assistantship of LCS was also partially supported by the Work Learn Program at UBC. RF-G acknowledges support from the Natural Sciences and Engineering Research Council of Canada (418438-13), the Canada Foundation for Innovation (30279), the Ontario Ministry of Economic Development and Innovation (ER14-10-170), the Ted Rogers Centre for Heart Research TBEP Seed Program, and the Canada First Research Excellence Fund—University of Toronto Medicine by Design. RF-G is the Tier II Canada Research Chair in Quantitative Cell Biology and Morphogenesis.

ORCID iDs

Lim C Siang  <https://orcid.org/0000-0002-0196-2354>

James J Feng  <https://orcid.org/0000-0002-7141-5823>

References

- [1] Irvine K D and Wieschaus E 1994 Cell intercalation during *Drosophila* germband extension and its regulation by pair-rule segmentation genes *Development* **120** 827–41
- [2] Butler L C, Blanchard G B, Kabla A J, Lawrence N J, Welchman D P, Mahadevan L, Adams R J and Sanson B 2009

- Cell shape changes indicate a role for extrinsic tensile forces in *Drosophila* germ-band extension *Nat. Cell Biol.* **11** 859
- [3] Sawyer J K, Choi W, Jung K-C, He L, Harris N J and Peifer M 2011 A contractile actomyosin network linked to adherens junctions by canoe/afadin helps drive convergent extension *Mol. Biol. Cell* **22** 2491–508
- [4] da Silva S M and Vincent J-P 2007 Oriented cell divisions in the extending germband of *Drosophila* *Development* **134** 3049–54
- [5] Lye C M, Blanchard G B, Naylor H W, Muresan L, Huisken J, Adams R J and Sanson B 2015 Mechanical coupling between endoderm invagination and axis extension in *Drosophila* *PLoS Biol.* **13** e1002292
- [6] Collinet C, Rauzi M, Lenne P-F and Lecuit T 2015 Local and tissue-scale forces drive oriented junction growth during tissue extension *Nat. Cell Biol.* **17** 1247–58
- [7] Tetley R J, Blanchard G B, Fletcher A G, Adams R J and Sanson B 2016 Unipolar distributions of junctional myosin II identify cell stripe boundaries that drive cell intercalation throughout *Drosophila* axis extension *Elife* **5** e12094
- [8] Bertet C, Sulak L and Lecuit T 2004 Myosin-dependent junction remodelling controls planar cell intercalation and axis elongation *Nature* **429** 667–71
- [9] Blankenship J T, Backovic S T, Sanny J S, Weitz O and Zallen J A 2006 Multicellular rosette formation links planar cell polarity to tissue morphogenesis *Dev. Cell* **11** 459–70
- [10] Fernandez-Gonzalez R, Simões S D M, Röper J-C, Eaton S and Zallen J A 2009 Myosin II dynamics are regulated by tension in intercalating cells *Dev. Cell* **17** 736–43
- [11] Zallen J A and Blankenship J T 2008 Multicellular dynamics during epithelial elongation *Semin. Cell Dev. Biol.* **19** 263–70
- [12] Zallen J A and Wieschaus E 2004 Patterned gene expression directs bipolar planar polarity in *Drosophila* *Dev. Cell* **6** 343–55
- [13] Tamada M, Farrell D L and Zallen J A 2012 Abl regulates planar polarized junctional dynamics through β -catenin tyrosine phosphorylation *Dev. Cell* **22** 309–19
- [14] Simões S D M, Mainieri A and Zallen J A 2014 Rho GTPase and Shroom direct planar polarized actomyosin contractility during convergent extension *J. Cell Biol.* **204** 575–89
- [15] Fernandez-Gonzalez R and Zallen J A 2011 Oscillatory behaviors and hierarchical assembly of contractile structures in intercalating cells *Phys. Biol.* **8** 045005
- [16] Fernandez-Gonzalez R and Zallen J A 2009 Cell mechanics and feedback regulation of actomyosin networks *Sci. Signaling* **2** pe78
- [17] Samarin S N, Ivanov A I, Flatau G, Parkos C A and Nusrat A 2007 Rho/Rho-associated kinase-II signaling mediates disassembly of epithelial apical junctions *Mol. Biol. Cell* **18** 3429–39
- [18] Simões S D M, Blankenship J T, Weitz O, Farrell D L, Tamada M, Fernandez-Gonzalez R and Zallen J A 2010 Rho-kinase directs bazooka/par-3 planar polarity during *Drosophila* axis elongation *Dev. Cell* **19** 377–88
- [19] Harris T J and Peifer M 2004 Adherens junction-dependent and -independent steps in the establishment of epithelial cell polarity in *Drosophila* *J. Cell Biol.* **167** 135–47
- [20] Paré A C, Vichas A, Fincher C T, Mirman Z, Farrell D L, Mainieri A and Zallen J A 2014 A positional toll receptor code directs convergent extension in *Drosophila* *Nature* **515** 523
- [21] Rauzi M, Verant P, Lecuit T and Lenne P-F 2008 Nature and anisotropy of cortical forces orienting *Drosophila* tissue morphogenesis *Nat. Cell Biol.* **10** 1401
- [22] Yu J C and Fernandez-Gonzalez R 2016 Local mechanical forces promote polarized junctional assembly and axis elongation in *Drosophila* *Elife* **5** e10757
- [23] Kong D, Wolf F and Großhans J 2017 Forces directing germ-band extension in *Drosophila* embryos *Mech. Dev.* **144** 11–22
- [24] Lan H, Wang Q, Fernandez-Gonzalez R and Feng J J 2015 A biomechanical model for cell polarization and intercalation during *Drosophila* germband extension *Phys. Biol.* **12** 056011
- [25] Fisher K H, Strutt D and Fletcher A G 2017 Integrating planar polarity and tissue mechanics in computational models of epithelial morphogenesis *Curr. Opin. Syst. Biol.* **5** 41–9
- [26] Fletcher A G, Cooper F and Baker R E 2017 Mechanocellular models of epithelial morphogenesis *Phil. Trans. R. Soc. B* **372** 20150519
- [27] Rauzi M, Lenne P-F and Lecuit T 2010 Planar polarized actomyosin contractile flows control epithelial junction remodelling *Nature* **468** 1110–5
- [28] Dicko M, Saramito P, Blanchard G B, Lye C M, Sanson B and Étienne J 2017 Geometry can provide long-range mechanical guidance for embryogenesis *PLoS Comput. Biol.* **13** e1005443
- [29] Trichas G *et al* 2012 Multi-cellular rosettes in the mouse visceral endoderm facilitate the ordered migration of anterior visceral endoderm cells *PLoS Biol.* **10** e1001256
- [30] Bambardekar K, Clément R, Blanc O, Chardès C and Lenne P-F 2015 Direct laser manipulation reveals the mechanics of cell contacts *in vivo* *Proc. Natl Acad. Sci. USA* **112** 1416–21
- [31] Farrell D L, Weitz O, Magnasco M O and Zallen J A 2017 SEGGA: a toolset for rapid automated analysis of epithelial cell polarity and dynamics *Development* **144** 1725–34
- [32] Efler J C, Kee Y-S, Berk J M, Tran M N, Iglesias P A and Robinson D N 2006 Mitosis-specific mechanosensing and contractile-protein redistribution control cell shape *Curr. Biol.* **16** 1962–7
- [33] Zulueta-Coarasa T and Fernandez-Gonzalez R 2018 Dynamic force patterns promote collective cell movements during embryonic wound repair *Nat. Phys.* **14** 750–8
- [34] Guillot C and Lecuit T 2013 Mechanics of epithelial tissue homeostasis and morphogenesis *Science* **340** 1185–9
- [35] Zallen J A and Zallen R 2004 Cell-pattern disordering during convergent extension in *Drosophila* *J. Phys. Condens. Matter* **16** S5073–80
- [36] Levayer R and Lecuit T 2012 Biomechanical regulation of contractility: spatial control and dynamics *Trends Cell Biol.* **22** 61–81
- [37] Levayer R and Lecuit T 2013 Oscillation and polarity of e-cadherin asymmetries control actomyosin flow patterns during morphogenesis *Dev. Cell* **26** 162–75
- [38] Munjal A, Philippe J M, Munro E and Lecuit T 2015 A self-organized biomechanical network drives shape changes during tissue morphogenesis *Nature* **524** 351–5

Supporting Information for “Modeling Cell Intercalation During *Drosophila* Germband Extension”

Lim C. Siang¹, Rodrigo Fernandez-Gonzalez^{2,3,4} and James J. Feng^{1,5*}

¹ Department of Chemical and Biological Engineering, University of British Columbia,
Vancouver, BC V6T 1Z3, Canada

² Institute of Biomaterials and Biomedical Engineering, University of Toronto, Toronto,
ON, M5S 3G9, Canada

³ Department of Cell and Systems Biology, University of Toronto, Toronto, ON, M5S 3G5,
Canada

⁴ Developmental and Stem Cell Biology Program, The Hospital for Sick Children, Toronto,
ON, M5G 1X8, Canada

⁵ Department of Mathematics, University of British Columbia, Vancouver, BC V6T 1Z2,
Canada

S1 Remodeling of adherens junctions

Experimental evidence suggests that adherens junctions (AJs) are actively disassembled on contracting AP edges and assembled on elongating DV edges. Although the molecular pathways are not completely clear, Rok and Abl enrichment is believed to promote AJ disassembly, while Baz, β -catenin and E-cad are involved in AJ assembly [1–3]. Of these proteins, only Rok and Baz are explicitly accounted for in our model; upon onset of PCP, they localize predominantly to the AP and DV edges, respectively [4]. As a simple device to produce the desired effect, we have chosen Baz to be the variable that controls AJ dynamics in our model. This is because its function and location are closely correlated with those of β -catenin and E-cad in establishing and stabilizing AJs [5], and negatively correlated with those of Abl and Rok in AJ disassembly [1, 2]. Thus, Baz enrichment on nascent DV edges can be used in the model as a trigger for AJ assembly, whereas its relative paucity on AP edges can be used to induce AJ disassembly, representing either the Rok or Abl pathway, or both [1, 2].

The mechanical effects of the AJs will be reflected by the passive elasticity of the cell edges. Disassembly of AJs facilitates contraction of AP edges. This is represented in our model by a resting length l_0 that shortens with the declining level of Baz. A shorter l_0 presents less elastic

*Corresponding author. E-mail: james.feng@ubc.ca

resistance to myosin-induced AP contraction. Conversely, the assembly of AJs on DV edges is modeled by an l_0 that lengthens as Baz rises, thereby contributing to the elongation of the nascent DV edges [6]. It is reasonable to expect a delay in the reaction of l_0 to variations in Baz, depending on the kinetics of AJ remodeling. For this we have used two different tanh profiles for $l_0(B)$ for the AP and DV edges (Fig. S1):

$$l_0(B) = \frac{l_0^{eq} + l_{min}}{2} + \frac{l_0^{eq} - l_{min}}{2} \cdot \tanh\left(\frac{B - B_{AP}}{b}\right) \quad (\text{for the AP edge}), \quad (\text{S1})$$

$$l_0(B) = \frac{l_0^{eq} + l_{min}}{2} + \frac{l_0^{eq} - l_{min}}{2} \cdot \tanh\left(\frac{B - B_{DV}}{b}\right) \quad (\text{for the DV edge}). \quad (\text{S2})$$

The parameters are designed such that both AP and DV edges assume a resting length of l_0^{eq} for large B and a minimum l_{min} for small B . The threshold values B_{AP} and B_{DV} are defined relative to the minimum $B_{min} = 0.368$ on the AP edge and maximum $B_{max} = 0.607$ on the DV edge, respectively, after PCP is established [4]. We have chosen $B_{AP} = 0.41$ and $B_{DV} = 0.57$, and a small $b = 0.0125$ to sharpen the transitions. The value $l_0^{eq} = 4.318 \mu\text{m}$ is determined in Sec. S3 below in connection to the pre-tension in the tissue. The minimum resting length is chosen to be $l_{min} = 0.08 \mu\text{m}$. During the simulation, Eq. (S1) is imposed on all AP and linked AP edges (including the sandwiched shoulder), whereas Eq. (S2) applies to all DV edges.

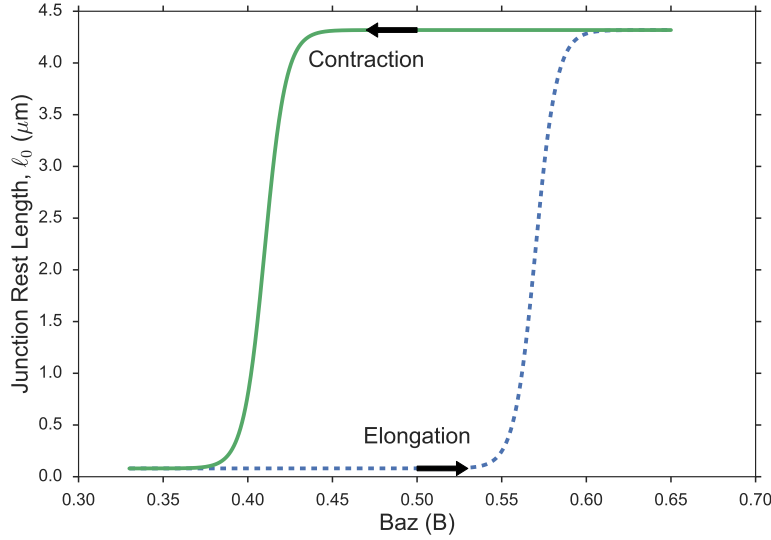


Figure S1: Tanh profiles for delayed reaction of the elastic resting length l_0 to Baz. The blue dashed curve represents the delayed growth of l_0 as B increases on the DV edge, while the green curve the delayed shortening of l_0 when B declines on the AP edge.

S2 Cross-correlation between oscillating neighbors

Germband cells exhibit a gentle oscillation corresponding to the early Stage 6 of experimental observations (e.g. Fig. 1 in Blankenship et al. [5]) due to a cyclic pulsation of their medial myosin. One cell's expansion or contraction tends to compress or pull on its neighbors. Thus, a negative correlation between the oscillation of neighbors is expected. Prior experiment indicated that although a broad distribution of correlations exists among the many pairs of neighbors, on average the neighbors exhibit predominantly anti-phase correlations [7]. In our model, we stagger the phase angle ϕ of our medial myosin pulses. More specifically, neighbors in the same row differ by $\pi/4$, while neighbors across rows differ either by $\pi/4$ or $\pi/2$ depending on the orientation of their line of centers (cf. Fig. 2 of the main text). We wish to verify that this scheme agrees with experimental observations of predominant anti-phase correlations.

For this purpose, we calculate the cross-correlation of the area variation between neighboring cells, with a time shift τ that ranges from 0 to the medial myosin period $T = 148$ s. For each cell, we define the area variation as the difference between the current area and its equilibrium value: $dA = A(t) - A_e$, A_e being the area of the hexagonal cell at its equilibrium edge length l_e of Table S1. Then the normalized cross-correlation of dA is calculated using the Python Numpy function *correlate* and averaged over all neighboring cell pairs. Figure S2 depicts the averaged correlation as a function of the time shift τ . The negative peak at $\tau = 0$ and positive peaks at approximately $\tau = \pm T/2$ indicate that anti-phase oscillation is predominant between neighbors with our setup, in agreement with experimental observations.

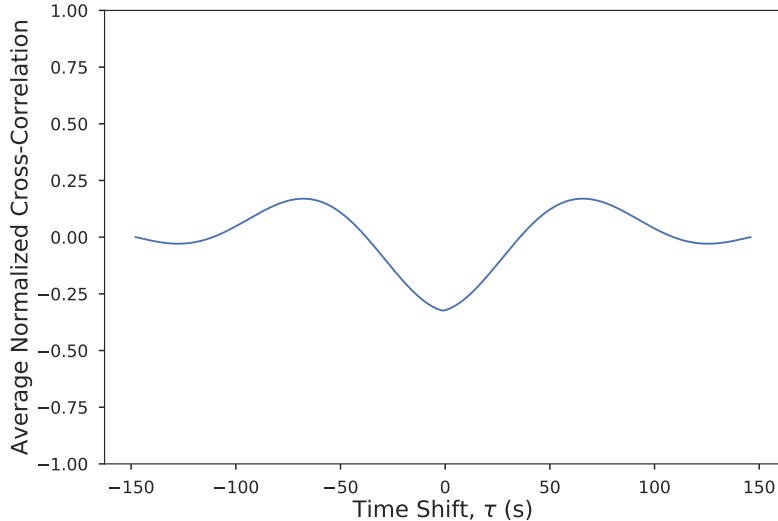


Figure S2: Average normalized cross-correlation of the area variation between neighboring cells in the tissue. τ is the time shift used in computing the cross correlation, and the negative peak close to $\tau = 0$ indicates anti-phase oscillation between neighbors. The period of medial myosin pulse is $T = 148$ s.

S3 Model parameters and numerics

The parameters in this model can be categorized into geometric, mechanical and kinetic parameters, and they are tabulated in Table S1 along with the sources. The evaluation of two parameters needs additional explanation, and this is given below.

| Parameter | Symbol | Description | Value | Sources |
|------------|--------------|--|------------------------------|----------------|
| Geometric | l_0^{eq} | equilibrium resting length | 4.318 μm | [8, 9] |
| | l_e | equilibrium edge length | 4 μm | [5, 7, 10] |
| | l_{min} | minimum edge length | 0.08 μm | [4] |
| | A_e | equilibrium cell area | 41.6 μm^2 | [7] |
| Mechanical | η | viscosity | 4.64 nN s μm^{-1} | [8, 9] |
| | μ | elastic modulus | 0.14 nN μm^{-1} | [4] |
| | β | myosin force coefficient | 0.324 nN | [8, 9, 11, 12] |
| | τ_{pre} | pre-tension | 0.27 nN | [8, 9] |
| | A_m | medial myosin amplitude | 1 | [7, 13] |
| | T | medial myosin period | 147 s | [7] |
| | α | pressure coefficient | 0.145 nN μm^{-2} | [14, 15] |
| Kinetic | q_r | Rok source term | 0.016 s^{-1} | [4] |
| | q_b | Baz source term | 0.016 s^{-1} | [4] |
| | k_1 | rate of promotion of myosin by Rok | 0.536 s^{-1} | [16] |
| | k_2 | rate of suppression of myosin by Baz | 0.48 s^{-1} | [4] |
| | k_3 | myosin off-rate constant | 0.216 s^{-1} | [17, 18] |
| | k_4 | force-dependent myosin detachment rate | 4.02 nN $^{-1}$ | [17, 18] |
| | k_r | rate of polarization of Shroom by Rok | 0.04 s^{-1} | [4] |
| | k_b | rate of Rok inhibition by Baz | 0.04 s^{-1} | [4] |

Table S1: Parameters used in our model.

The pre-tension τ_{pre} . It is known that the germband is under tension even prior to the onset of convergent extension. Bambardekar *et al.* [8] measured such tension on cell edges of different orientations in different stages of embryonic development. In particular, their Fig. 2C suggests a more or less isotropic pre-tension on the order of $\tau_{pre} = 0.05$ nN at the end of stage 5. A less direct estimation can also be made from the data of Rauzi *et al.* [9], Fig. 6e. After laser ablation, the retraction speed for relaxed cell edges (say 4-6 μm in length) is about 0.03 $\mu\text{m/s}$, half of that for contracting AP edges (~ 0.07 $\mu\text{m/s}$). Thus, the tension on the relaxed edges should be about half of the tension on the contracting ones, which averages to about 0.324 nN [8]. This gives $\tau_{pre} \sim 0.16$ nN. In the model, we have found that our simple polygonal cell tends to develop transient concave shapes if the pre-tension is too low. In view of the experimental data and this requirement, we have chosen $\tau_{pre} = 0.27$ nN.

The equilibrium resting length l_0^{eq} . As indicated by Eqs. (S1, S2), l_0^{eq} is the resting length for the elastic cell edges when its Baz level attains the maximum B_{max} , which is also the ‘‘equilibrium’’ level before the onset of PCP when a low Shroom $S_e = 0.5$ is imposed on all edges. In this equilibrium state discussed in Sec. 2.4 of main text, the cell edge contracts to an equilibrium length

$l_e = 4 \mu\text{m}$ under the equilibrium myosin m_e . Meanwhile, the edge tension should be the prescribed pre-tension τ_{pre} specified above. This condition determines the l_0^{eq} parameter:

$$\tau_{\text{pre}} = \beta m_e + \mu(l_e - l_0^{eq}), \quad (\text{S3})$$

which gives us $l_0^{eq} = (\beta m_e - \tau_{\text{pre}})/\mu + l_e = 4.318 \mu\text{m}$.

The computational setup and techniques are as follows. Our model germband tissue consists of a total of 52 cells, 183 edges and 132 vertices. Mathematically, therefore, our model comprises 916 ODEs with 732 equations describing four proteins on 183 edges, 132 ODEs describing the mechanical motion of the vertices and 52 equations describing the dynamics of medial myosin in the cells. The temporal evolution of the 52-cell tissue is investigated by solving the differential equations using a second-order Runge-Kutta method. The time step has been varied to study temporal resolution, and $\Delta t = 0.01 \text{ s}$ is shown to be sufficiently fine. The simulation lasts 3000 s or 3×10^5 time steps to reflect the typical germband extension time scale reported in the literature. Additional rules defining the probabilistic activation of T1 transitions and rosette formations, along with tissue-level features such as PMI modeling are calculated and applied on the vertices, edges and cells at each time step, where appropriate.

The simulation is written in the Python programming language. The geometry of the tissue is represented by a half-edge mesh data structure for efficient computation and manipulation of tissue topology required for T1 transitions and rosette resolution [19, 20]. The mesh consists of a set of vertices, edge and cell objects, with topological relations stored between them. Additional attributes required for the model such as kinetic and mechanical data are also stored in the mesh objects.

S4 Boundary treatment

Our model tissue is connected to the surrounding tissue by cables bearing a force F_{cable} that is constant in time but may vary among the cables. These must be chosen so as to maintain mechanical equilibrium at the start of the simulation. In addition, the left and right boundary vertices are assigned additional outward movement to mimic the effect of posterior midgut invagination (PMI) [21].

As shown in Fig. 2 of the main text, we have two kinds of boundary vertices in the model. Convex vertices are connected to two cell edges and do not have force balance unless an external cable is connected to it. On such cables a constant force of $F_{\text{cable}} = \tau_{\text{pre}}$ will maintain perfect force balance; it is as if the external cable serves as an ordinary edge. Concave vertices are connected to 3 edges, and the pre-tension on them would balance each other if the external cable carries zero force. An additional factor is the pulsating medial myosin, which adds a radially inward force that averages to $\beta A_m/2$ over each cycle. To account for this, we increase the cable force to $F_{\text{cable}} = \tau_{\text{pre}} + \beta A_m/2$ on cables connected to convex vertices, and $F_{\text{cable}} = \beta A_m/2$ on cables connected to concave vertices.

We model PMI using the experimental data of Lye *et al.* [21]. The strain rate of each cell is provided in units of pp/min, or “proportion per minute”, showing relative percentage changes in cell length relative to the *current length*. For the anterior and posterior portions of the tissue, the strain rates are given in their Fig. 1F and Fig. 1F’, respectively. We fit the anterior data using the following piecewise linear function of time t , in minutes:

$$\Delta x_l = \begin{cases} 0.0035t & t < 10 \\ -0.0032t + 0.0705 & 10 \leq t < 20 \\ 0.00625 & t \geq 20 \end{cases} \quad (\text{S4})$$

Similarly, we fit the posterior data of Fig. 1F’ with:

$$\Delta x_r = \begin{cases} 0.0031t - 0.0125 & t < 10 \\ -0.0008t + 0.0266 & t \geq 10 \end{cases} \quad (\text{S5})$$

At the start, we divide our tissue horizontally into a left half and a right half, corresponding to the anterior and posterior portion in Lye *et al.* [21]. Then during intercalation, we apply the strain rates above to these two halves. The length of each portion is measured between the centroids of the leftmost and rightmost cells, and designated as $\ell_l(t)$ and $\ell_r(t)$, respectively. Thus, the tissue elongation in each time step dt of the simulation, due to PMI and the shape change of each cell, is calculated by adding up the contributions from each half:

$$\Delta x = (\Delta x_l \ell_l + \Delta x_r \ell_r) \times \frac{dt}{60}, \quad (\text{S6})$$

where the division by 60 convert dt in seconds into minutes. In each time step of the simulation, we apply an additional leftward movement of $\frac{\Delta x}{2}$ on the left boundary vertices of our model tissue, and the same amount of rightward movement to the right boundary vertices. Thus, the additional elongation due to PMI is incorporated into the model.

Note that Lye *et al.* [21] reported spatial heterogeneity in the amount of cell length change, with greater cell elongation toward the posterior of the embryo, where the PMI takes place. In our model tissue, all vertices are free to move in space, and it is not possible to impose and maintain a greater strain in the posterior half. The cells at the left and right borders do deform more than those in the interior (see Movies 1 and 3), and this effect is symmetric between the anterior and posterior halves. The spatially inhomogeneous strain observed *in vivo* suggests that the germband must interact mechanically differently with the surrounding tissue in the anterior and posterior. Such a feature is not included in the current model.

S5 Frequency of the onset of T1 and rosette events

Stochasticity for the onset of AP contraction is modeled as a homogeneous Poisson process. The Poisson rate parameter, λ , or equivalently, the average time interval between consecutive onsets of AP contraction, is estimated from experimental data of Tamada *et al.* [2]. In their Fig. 3B, the authors plotted the number of neighbor exchange events per cell accumulated in time. Taking the “neighbor exchange event” to be the *completion* of AP contraction during T1 transitions, we estimate the rate of the *onset* of AP contraction by shifting the curve to the left by 8 minutes, which is the average AP contraction time reported by Blakenship *et al.* [5]. The slope of the shifted curve at $t = 0$ is the initial rate of onset of T1 events per cell, which gives us a Poisson parameter of 0.05 T1 events/cell per minute. For our 52-cell model, the rate parameter is $\lambda = 0.05 \times 52 = 2.6$ T1 events per minute. Similarly, for the rate of rosette formation, we apply the same methodology on Fig. 3C of [2], shifting the curve by 10.5 minutes [5] and obtained an initial rate of 0.026 rosette per cell per minute.

Numerically, we multiply the frequency λ to the size of the solver’s time step dt to obtain expected number of events happening within the time interval dt . Then according to the Poisson distribution, the probability of zero event happening within dt will be $e^{-\lambda dt}$, and that of at least one event happening will be $1 - e^{-\lambda dt}$. In each time step, we sample a random floating-point number uniformly from the interval $[0, 1]$. If the sampled number is less than $1 - e^{-\lambda dt}$, then a spatially random available AP edge is selected for contraction.

S6 Rosette resolution

We distinguish clockwise and counterclockwise configurations of rosettes. A clockwise rosette starts with a sandwiched shoulder in the upper-left to lower-right direction (Fig. S3a). After the linked AP edges contract to the critical length, we rotate them clockwise into a nascent DV edge comprising three segments. A counterclockwise rosette, in contrast, starts with a sandwiched shoulder in the lower-left to upper-right direction (Fig. S3b). The linked AP edges are rotated counterclockwise into the DV edge. There are multiple possibilities for reattaching cell edges onto the nodes of the new DV edge. We have designed our resolution scheme to ensure that the sandwiched shoulder should separate the same neighboring cells as before the transformation. In Fig. S3(a), for example, the shoulder $\overline{v_B v_C}$ separates cells C_C and C_F . In Fig. S3(b), the neighboring cells are C_B and C_E . This way, the clockwise and counterclockwise rosettes are resolved into a uniquely defined configuration after the transformation, which can then proceed to elongate along the AP axis.

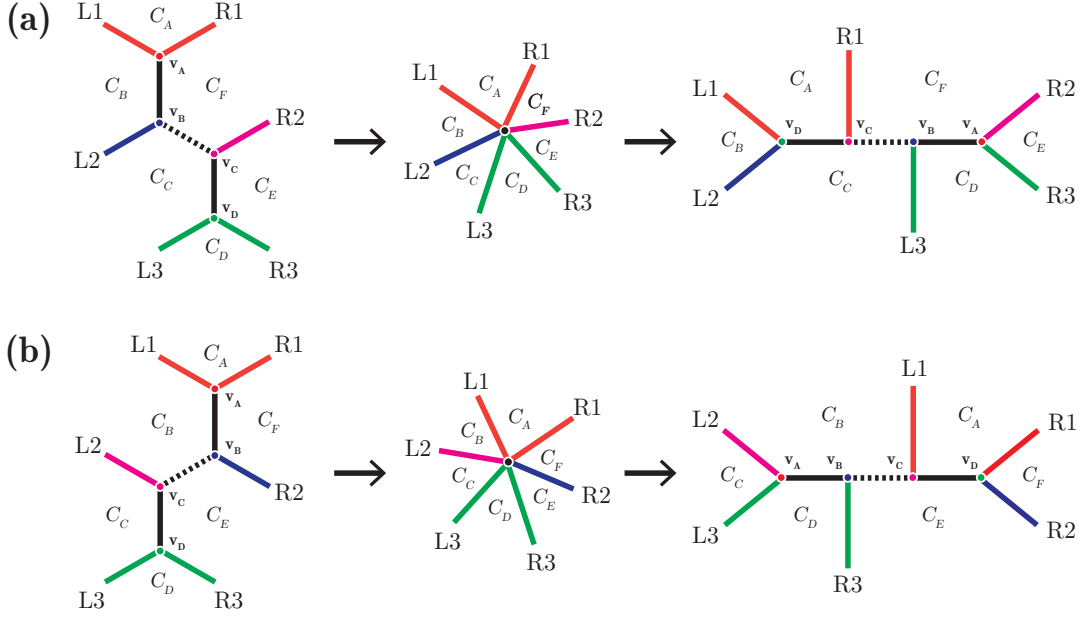


Figure S3: Six-cell rosette formation and resolution scheme for (a) clockwise and (b) counterclockwise configurations of rosette structures in our model. Cells are labeled C_i , vertices are labeled v_i , edges on the left and right half of the plane before resolution are labeled L_i and R_i respectively. The dotted line indicates the sandwiched shoulder between two contracting AP edges.

S7 Evolution of protein levels and forces on active edges

In our model, planar cell polarity (PCP) initiates when an AP edge is selected for contraction. Through a T1 transition or a rosette process, the AP edge or edges turn into a DV edge or edges. The development of the PCP in terms of the Rok, Baz and Myo-II distributions is largely the same as predicted by the simpler model of Lan *et al.* [4]. Figure S4 illustrates the temporal evolutions on the AP and DV edge during a representative T1 transition. At $t \sim 660$ s, the AP edge is selected for contraction. The elevated Shroom prompts a rise in Rok and decline in Baz. Subsequently Myo-II rises as well, and the myosin contraction force shortens the AP edge. The T1 transition occurs at $t \sim 1090$ s. On the new DV edge Rok and Myo-II fall while Baz rises. The elongation of the DV edge ends at $t \sim 1350$ s.

Figure S5 analyzes the makeup of the edge forces during T1 transition. The AP contraction is dominated by the active junctional myosin force f_{my} on the AP edge against the resistance force f_{SH} on the shoulder edges (Fig. S5a). The medial myosin force f_m plays a secondary role in assisting the contraction. The decline in elastic resistance around $t = 740$ s reflects the junctional disassembly, caused by the enrichment in Rok and loss in Baz due to PCP [1,22]. Our model mimics the loss of adherens junctions by a shrinking rest length l_0 for the passive elasticity, which relieves the compressive elastic force and even turns it into a tensile force later to assist AP constriction. During DV elongation (Fig. S5b), the driving forces are the shoulder junctional myosin force and the medial myosin force from the cells anterior and posterior to the DV edge. The resistance comes

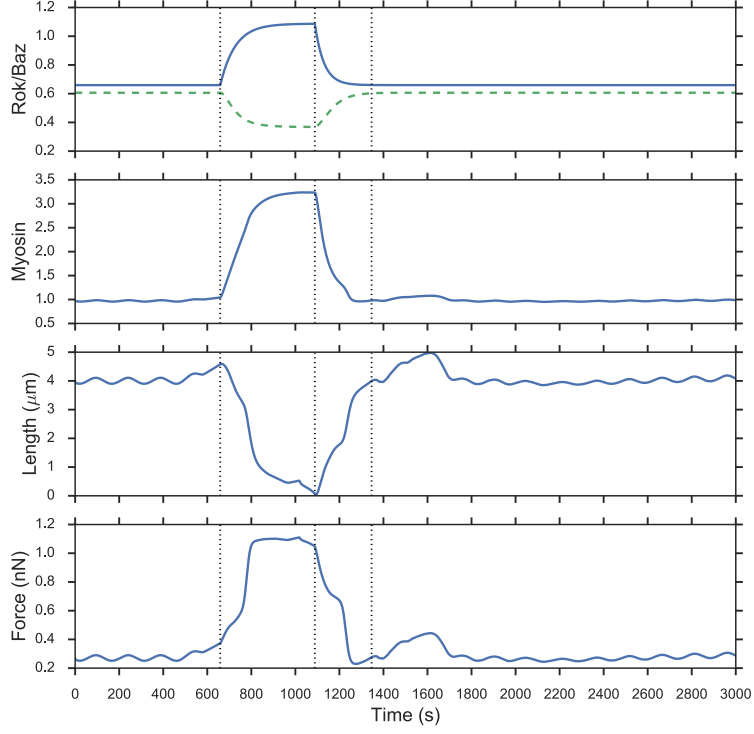


Figure S4: Temporal evolution of the key proteins on a representative edge (edge 166 between vertices 60 and 77) selected for contraction and T1 transition (solid line for Rok and dashed line for Baz in top panel), along with its length and total force on it. The vertical dashed lines indicate three key times of the process: the onset of PCP ($t \sim 660$ s), the swap of neighbors ($t \sim 1090$ s, when the AP edge turns into a DV edge) and the end of DV elongation ($t \sim 1350$ s).

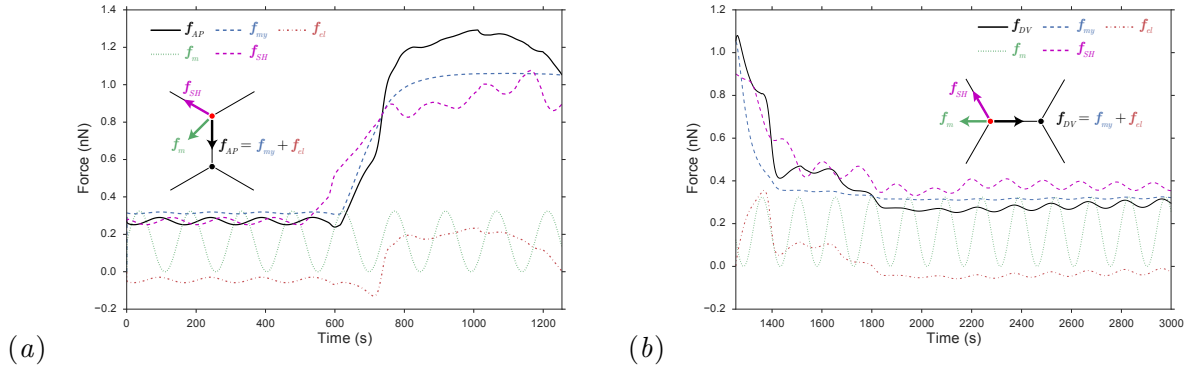


Figure S5: Analysis of the forces acting on the AP and DV edges during T1 transition. (a) The various forces acting on the top vertex of the AP edge. The total force on the AP edge is the sum of the myosin and elastic forces: $f_{AP} = f_{my} + f_{el}$. (b) The various forces acting on the left vertex after the DV edge is created. The total force on the DV edge is the sum of the myosin and elastic forces: $f_{DV} = f_{my} + f_{el}$.

mainly from the junctional myosin contraction on the DV edge and the medial myosin of the two cells on top and below the DV edge (not plotted). The initially high level of Myo-II on the DV edge

quickly declines in time in reaction to the PCP. The shoulder force declines in response. Another consequence of the PCP is the rising Baz on the DV edge and the lengthening l_0 that mimics the buildup of new AJs [1]. This relieves the elastic tension as the DV edge grows and facilitates DV elongation. These observations are similar to those of Lan *et al.* [4], except for the new mechanism of junctional remodeling in terms of l_0 . The prominent role of the medial myosin in elongating the DV edge has since been confirmed by experiments [23, 24].

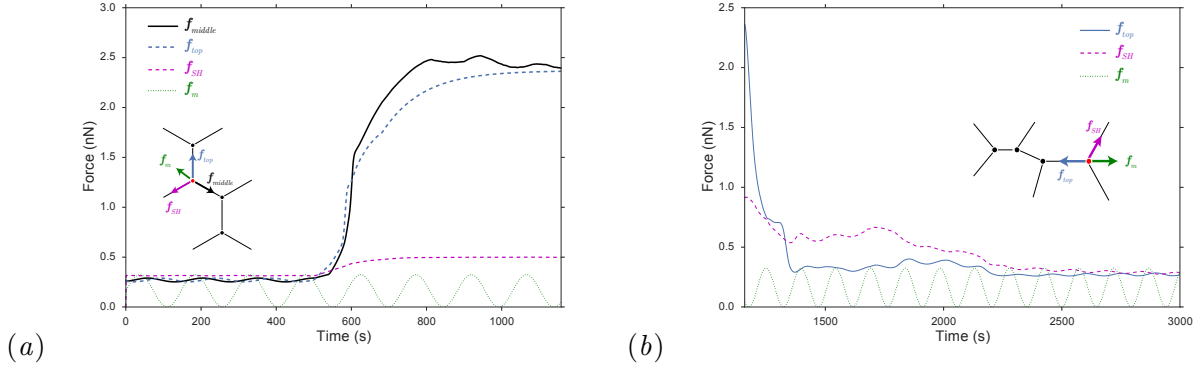


Figure S6: Analysis of the forces governing rosette formation and resolution transition. (a) The various forces acting on a middle vertex of the linked AP edge during rosette formation. (b) The various forces acting on the rightmost vertex during rosette resolution. The force on an edge, such as f_{top} , f_{SH} and f_{middle} , are each the sum of the myosin and elastic forces on that edge.

For rosettes, a similar force analysis can be done. As the linked AP edge contracts, the tensile forces on its 3 segments are mostly due to myosin. They are comparable in magnitude (e.g. $f_{top} \sim f_{middle}$ in Fig. S6a), and are undoubtedly the driving force of the AP contraction to a vertex. The resistance mainly comes from the shoulder edges connected to the contracting edges, such as f_{SH} plotted here, as well as the passive elasticity in the linked AP edge. During rosette resolution, the shoulder tension f_{SH} as well as the medial myosin force f_m in the cell to the left and right of the elongating edges are the main driving forces for the elongation. The main resistance is the tension f_{top} on the DV edge, due mostly to myosin contraction. The high Baz on these edges promotes and stabilizes adherens junctions. This is reflected in our model by a resting length l_0 that increases with Baz, thus alleviating the elastic tension that would have hampered DV elongation. To sum up the force analysis of rosettes, the essential features are similar to T1 transitions, although the forces are larger and the morphological changes are more complex.

S8 Myosin enrichment on stretched cell edges

The formation of a rosette requires much stronger anisotropic myosin contraction than that required of the T1 transition. As a potential factor for this contraction, recent experiments suggest that stretching of a cell edge to a large strain or strain rate may predispose the edge to a strong surge of myosin recruitment afterwards [13, 25, 26]. This is a potential mechanism for the strong contraction

of the linked AP edge. In the setup of our model, two contracting AP edges elongate a shoulder edge sandwiched in between. We wonder if the stretched shoulder could subsequently acquire an elevated level of myosin through the strain- or strain-rate-based mechanism suggested by the experiments.

We have tested this hypothesis by incorporating a strain or strain-rate effect into the kinetic equation for myosin (the same equation appears as Eq. 3 in the main text):

$$\frac{dm}{dt} = k_1 R - k_2 m B - k^- m. \quad (\text{S7})$$

First, following [26], we introduced a new myosin attachment term to the righthand side of the form $k^+ m_c$, where m_c represents cytoplasmic myosin and the activation rate k^+ is modeled as a Hill function of the strain s . With this mathematical formulation, the myosin on the shoulder rises markedly while it is stretched, but the shoulder edge fails to contract afterwards as intended. The main reason is that k^+ sets up a negative feedback loop between the strain and myosin levels. As the stretched shoulder edge starts to contract due to its myosin buildup, the strain on the edge drops. This instantly reduced k^+ and causes the myosin level to decline, preventing sustained, large-strain contraction.

In another attempt, we added a strain-rate term to the myosin detachment rate k^- in the last term of Eq. (S7). In its original form, $k^- = k_3 e^{-k_4 f}$ is suppressed by tensile force f on the edge. Thus the tension inhibits myosin detachment, and in turn produces more tension through a well-known positive feedback loop [13]. Zulueta-Coarasa and Fernandez-Gonzalez [26] observed that myosin dynamics are regulated by both strain and tension during embryonic wound closure. This motivated us to add a strain-rate term into the exponent:

$$k^- = k_3 e^{-k_4 f + k_5 g}, \quad (\text{S8})$$

where $g = (dl/dt)/l$ is the strain rate of the edge, $l(t)$ being the instantaneous edge length. Furthermore, when g turns negative on a shrinking edge, we put g to 0 to avoid depressing myosin. Unfortunately, this scheme did not even produce a strong boost of myosin on the shoulder edge. The reason is that for the parameters being used, the tension-based feedback effect is already very effective; it suppresses the myosin detachment to a low level such that further suppression does little to boost the myosin level.

The failure of the attempts above probably reflects the inadequacy of our mathematical formalism. We model the myosin enrichment as dependent on the instantaneous strain or strain rate. Experiments suggest, however, that the myosin surge follows stretching of an edge with a delay of 4 – 10 min [13, 26]. Pharmacological inhibition tests point to stretch-activated ion channels as a key mediator of the strain effect on myosin. The kinetics of this pathway, with further signaling downstream of the ion channel activation, offer ample possibility for introducing such a delay. Thus, replacing the instantaneous reactions tested above with a relaxation-based effect, akin to viscoelasticity, may provide a more satisfactory mathematical description of the strain effect.

S9 Supplemental Movies

Three supplemental movies can be downloaded from the article’s home page. Below are their captions.

Movie 1: The tissue undergoing T1 transition only. This special case is designed to explore the role of T1 in the absence of rosettes. The purple vertices at the ends are subject to additional movement due to posterior midgut invagination. When an AP edge is selected for contraction, its vertices are marked in green. After T1 transition, the vertices of the new DV edge are marked in blue.

Movie 2: Magnified view of the formation and resolution of a single rosette. When the two AP edges are selected for contraction at 499 s and 501 s, their vertices are marked in red. When the shoulder in between is selected so the three form a linked AP edge at 538 s, its four vertices are labeled by different colors that remain through the resolution phase as well.

Movie 3: Full simulation of the tissue deformation with stochastic T1 transitions and rosettes. Isolated AP edges are indicated by green vertices, which turn blue after the T1 transitions. Linked AP edges and the resulting DV edges following rosette resolution are marked in red throughout.

References

- [1] S. d. M. Simões, J. T. Blankenship, O. Weitz, D. L. Farrell, M. Tamada, R. Fernandez-Gonzalez, J. A. Zallen, Rho-kinase directs bazooka/par-3 planar polarity during *Drosophila* axis elongation, *Dev. Cell* 19 (3) (2010) 377–388.
- [2] M. Tamada, D. L. Farrell, J. A. Zallen, Abl regulates planar polarized junctional dynamics through β -catenin tyrosine phosphorylation, *Dev. Cell* 22 (2) (2012) 309–319.
- [3] J. A. Zallen, J. T. Blankenship, Multicellular dynamics during epithelial elongation, *Semin. Cell Dev. Biol.* 19 (3) (2008) 263–270.
- [4] H. Lan, Q. Wang, R. Fernandez-Gonzalez, J. J. Feng, A biomechanical model for cell polarization and intercalation during *Drosophila* germband extension, *Phys. Biol.* 12 (5) (2015) 056011.
- [5] J. T. Blankenship, S. T. Backovic, J. S. Sanny, O. Weitz, J. A. Zallen, Multicellular rosette formation links planar cell polarity to tissue morphogenesis, *Dev. Cell* 11 (4) (2006) 459–470.
- [6] B. Baum, M. Georgiou, Dynamics of adherens junctions in epithelial establishment, maintenance, and remodeling, *J. Cell Biol.* 192 (2011) 907–917.

- [7] R. Fernandez-Gonzalez, J. A. Zallen, Oscillatory behaviors and hierarchical assembly of contractile structures in intercalating cells, *Phys. Biol.* 8 (4) (2011) 045005.
- [8] K. Bambardekar, R. Clément, O. Blanc, C. Chardès, P.-F. Lenne, Direct laser manipulation reveals the mechanics of cell contacts in vivo, *Proc. Natl. Acad. Sci. U.S.A.* 112 (5) (2015) 1416–1421.
- [9] M. Rauzi, P. Verant, T. Lecuit, P.-F. Lenne, Nature and anisotropy of cortical forces orienting *Drosophila* tissue morphogenesis, *Nat. Cell Biol.* 10 (12) (2008) 1401.
- [10] M. Rauzi, P.-F. Lenne, T. Lecuit, Planar polarized actomyosin contractile flows control epithelial junction remodelling, *Nature* 468 (7327) (2010) 1110–1104.
- [11] M. Vinzenz, M. Nemethova, F. Schur, J. Mueller, A. Narita, E. Urban, C. Winkler, C. Schmeiser, S. A. Koestler, K. Rottner, et al., Actin branching in the initiation and maintenance of lamellipodia, *J Cell Sci* 125 (11) (2012) 2775–2785.
- [12] T. Q. Uyeda, S. J. Kron, J. A. Spudich, Myosin step size: estimation from slow sliding movement of actin over low densities of heavy meromyosin, *Journal of molecular biology* 214 (3) (1990) 699–710.
- [13] R. Fernandez-Gonzalez, S. d. M. Simões, J.-C. Röper, S. Eaton, J. A. Zallen, Myosin II dynamics are regulated by tension in intercalating cells, *Dev. Cell* 17 (5) (2009) 736–743.
- [14] T. Bittig, O. Wartlick, A. Kicheva, M. González-Gaitán, F. Jülicher, Dynamics of anisotropic tissue growth, *New Journal of Physics* 10 (6) (2008) 063001.
- [15] P. P. Girard, E. A. Cavalcanti-Adam, R. Kemkemer, J. P. Spatz, Cellular chemomechanics at interfaces: sensing, integration and response, *Soft Matter* 3 (3) (2007) 307–326.
- [16] M. Amano, M. Ito, K. Kimura, Y. Fukata, K. Chihara, T. Nakano, Y. Matsuura, K. Kaibuchi, Phosphorylation and activation of myosin by rho-associated kinase (rho-kinase), *Journal of Biological Chemistry* 271 (34) (1996) 20246–20249.
- [17] C. Veigel, J. E. Molloy, S. Schmitz, J. Kendrick-Jones, Load-dependent kinetics of force production by smooth muscle myosin measured with optical tweezers, *Nat. Cell Biol.* 5 (11) (2003) 980–986.
- [18] M. Kovács, K. Thirumurugan, P. J. Knight, J. R. Sellers, Load-dependent mechanism of nonmuscle myosin 2, *Proc. Natl. Acad. Sci. U.S.A.* 104 (24) (2007) 9994–9999.
- [19] L. Kettner, Using generic programming for designing a data structure for polyhedral surfaces, *Computational Geometry* 13 (1) (1999) 65–90.
- [20] M. Botsch, S. Steinberg, S. Bischoff, L. Kobbelt, OpenMesh: A Generic and Efficient Polygon Mesh Data Structure, in: *OpenSG Symposium 2002*, 2002.

- [21] C. M. Lye, G. B. Blanchard, H. W. Naylor, L. Muresan, J. Huisken, R. J. Adams, B. Sanson, Mechanical coupling between endoderm invagination and axis extension in *Drosophila*, PLoS Biol. 13 (11) (2015) e1002292.
- [22] S. N. Samarin, A. I. Ivanov, G. Flatau, C. A. Parkos, A. Nusrat, Rho/Rho-associated kinase-II signaling mediates disassembly of epithelial apical junctions, Mol. Biol. Cell 18 (2007) 3429–3439.
- [23] C. Collinet, M. Rauzi, P.-F. Lenne, T. Lecuit, Local and tissue-scale forces drive oriented junction growth during tissue extension, Nat. Cell Biol. 17 (10) (2015) 1247–1258.
- [24] J. C. Yu, R. Fernandez-Gonzalez, Local mechanical forces promote polarized junctional assembly and axis elongation in *Drosophila*, Elife 5 (2016) e10757.
- [25] J. C. Effler, Y.-S. Kee, J. M. Berk, M. N. Tran, P. A. Iglesias, D. N. Robinson, Mitosis-specific mechanosensing and contractile-protein redistribution control cell shape, Curr. Biol. 16 (2006) 1962–1967.
- [26] T. Zulueta-Coarasa, R. Fernandez-Gonzalez, Dynamic force patterns promote collective cell movements during embryonic wound repair, Nature Phys. in press.